applied sciences

MDPI

Article

Wind Turbine Enhancement via Active Flow Control Implementation

Marc Lahoz, Ahmad Nabhani, Mohammad Saemian and Josep M. Bergada *

Fluid Mechanics Department, Universitat Politècnica de Catalunya, 08034 Barcelona, Spain; marc.lahoz10@gmail.com (M.L.); ahmad.nabhani@upc.edu (A.N.); mohammad.saemian@upc.edu (M.S.)
* Correspondence: josep.m.bergada@upc.edu; Tel.: +34-937-398-771

Abstract: The present research enhances the efficiency of an airfoil section from the DTU-10MW Horizontal Axis Wind Turbine (HAWT) via Active Flow Control (AFC) implementation and when using synthetic jets (SJ). The flow around two airfoil sections cut along the wind turbine blade and for a wind speed of 10 m/s is initially simulated using the CFD-2D-RANS-Kω-SST turbulence model, from where the time-averaged boundary layer separation point and the associated vortex shedding frequency are obtained. On a second stage of the paper, and considering one of the two airfoil sections, the boundary layer separation point previously determined is used to locate the SJ groove as well as the groove width; the three remaining AFC parameters, momentum coefficient, jet inclination angle, and jet pulsating frequency, are parametrically optimized. Thanks to the energy assessment presented in the final part of the paper, the study shows that a considerable power increase of the airfoil section can be obtained when attaching the former separated boundary layer. The extension of the optimization process to the rest of the blade sections where the boundary layer is separated would lead to an efficiency increase of the HAWT. The Reynolds numbers associated to the respective airfoil sections analyzed in the present manuscript are $Re = 14.088 \times 10^6$ and $Re = 14.877 \times 10^6$, the characteristic length being the corresponding chord length for each airfoil.

Keywords: computational fluid dynamics (CFD); active flow control (AFC); synthetic jet; boundary layer; aerodynamic efficiency; parametric optimization

check for updates

Citation: Lahoz, M.; Nabhani, A.; Saemian, M.; Bergada, J.M. Wind Turbine Enhancement via Active Flow Control Implementation. *Appl. Sci.* **2024**, *14*, 11404. https://doi.org/10.3390/app142311404

Academic Editor: Zhaosheng Yu

Received: 14 November 2024
Revised: 1 December 2024
Accepted: 5 December 2024
Published: 7 December 2024

Copyright: © 2024 by the authors. Licensee MDPI, Basel, Switzerland. This article is an open access article distributed under the terms and conditions of the Creative Commons Attribution (CC BY) license (https://creativecommons.org/licenses/by/4.0/).

1. Introduction

The number of articles tackling Active Flow Control (AFC) applied to airfoils is rising sharply [1–5]. The AFC technology basically consists of adding or subtracting momentum to/from the main flow in order to interact with the boundary layer and delay its separation. Its main advantage over passive flow control approaches is that it is not creating a drag penalty in off-design conditions.

The different AFC techniques were divided by Cattafesta and Sheplak [6] into three categories: (1) moving body actuators [7], (2) plasma actuators [8–11], and (3) fluidic actuators (FA). From these three categories, FA are the only ones capable of generating large momentum coefficients, and this is why they were chosen for the present research. In some particular FA designs, the origin of the self-sustained oscillations was recently unveiled in [12–14]. From the different FA, Zero Net Mass Flow Actuators (ZNMFA), also called synthetic jet actuators (SJA), have the advantage of not requiring external fluid supply, being particularly effective in controlling the separation of the boundary layer [15–18]. The use of pulsating flow has the advantage of coupling with the boundary's layer natural instabilities and so being more energetically efficient [19–21]. In fact, in order to minimize the energy required in AFC implementations, it is needed to somehow optimize the different parameters associated with each particular AFC application; nowadays, the most common methodology employed to tune the AFC-associated parameters is a parametric optimization, although the use of optimizers is increasingly accepted [22–24].

Active Flow Control implementation in Vertical (VAWT) and Horizontal Axis Wind Turbines (HAWT) is recently gaining momentum [1,5,25–32], although so far, the bases to optimize the five AFC-associated parameters along the blade are not being established. Among the different devices employed in AFC applications on (WT), synthetic jets (SJ) appear to be particularly effective, as they combine the use of periodic forcing (blowing/suction) with a sufficiently large momentum coefficient C_μ, which is defined as $C_\mu = (h\rho_{jet}(U_j^2)\sin\theta)/(C\rho_\infty(U_\infty^2))$, where h is the jet width, ρ_{jet} and ρ_∞ are the jet and far field densities, respectively, U_j is the maximum jet velocity, C is the airfoil chord, U_∞ is the free-stream velocity, and θ is the jet inclination angle with respect to the adjacent surface, a combination that appears to be particularly effective in delaying the boundary layer separation. The non-dimensional frequency associated with periodic forcing is defined as $F^+ = fC/U_\infty$, with f being the boundary layer natural dimensional frequency.

A thorough experimental work employing SJ on wind turbine blade sections was undertaken by [25], where it was established that AFC-SJ was capable of delaying airfoil stall and proved that a significant reduction of wind turbine start-up velocity was possible. In [26,33], SJ were employed to control the fluid flow vibration induced on turbine blades; they observed that the boundary layer reattachment obtained when applying AFC was having associated lower amplitude lift and drag dynamic coefficients and with it smaller structural vibrations. The use of SJ to enhance the performance of VAWT was experimentally addressed in [27]; they obtained a considerable reduction of the noise generated while increasing the power generated by the turbine as well as its safety. Similar experimental studies using SJ but on a VAWT S809 and a HAWT S809 airfoil were performed by [28] and [31], respectively. The former study demonstrated that lift, drag, and pitching moment hysteresis could be significantly reduced. In the later research they observed that a 10.6% power input reduction to drive the rotor was achieved when a total of 20 SJA along each blade were employed.

Due to the high cost associated with experimental studies and the increasing trustworthiness of the computational simulations, the current tendency is to simulate the performance of any device. In this direction are going the 2D-URANS numerical simulations on VAWT performed by [1,29]. In both cases a straight-bladed WT was investigated, although the second one was of Darrieus type. Three different SJ locations were investigated in the later research, while in the former, not just the location but also the number of holes of the SJ were considered. A net power increase was obtained in both investigations; a power coefficient increase of 15.2% was obtained in [1]. A numerical investigation on the S809-HAWT airfoil aerodynamic enhancement using SJ was undertaken by [30]. Lift increase was observed for a wide range of injected flow angles. As previously performed by [1], Wang et al. [32] placed the SJA at the airfoil trailing edge and numerically studied the aerodynamic characteristics improvement on a straight-bladed VAWT. They evaluated the performance of several configurations of dual synthetic jets actuators (DSJA) to improve the power capacity of the WT and observed that the power coefficient could be increased by 58.87% when the juxtaposition-type DSJA was used. One of the latest pieces of research on AFC applications to HAWT with S809 airfoils is the one performed experimentally by Maldonado et al. [5]. Two rotors with blade aspect ratios of 7.79 and 9.74 and having 20 SJA distributed along the span of each blade were analyzed at four different turning speeds and three pitch angles. The rotor with a higher aspect ratio was found to be more aerodynamically efficient, and thanks to the use of AFC, unsteady bending and unsteady torsion could be reduced by 36.5% and 22.9%, respectively.

In all the research just presented on WT, the five AFC parameters—SJ position, width, injection angle, frequency, and momentum coefficient—were chosen without performing a previous optimization, which appears to be the necessary task if minimum energy for the actuation is to be used. In fact, when aiming to optimize the different AFC parameters, the following considerations gathered from previous investigations are needed.

When experimentally studying the flow control on the NACA-0025 airfoil at $Re = 10^5$ and AoA = 5°, Goodfellow et al. [34] observed that the momentum coefficient was the

primary control parameter. When analyzing the effect of jet position in controlling the boundary layer separation [35], it was observed that the maximum effectiveness was obtained when placing the jet groove close to the boundary layer separation point, either downstream or upstream. The same observations were made by Amitay et al. [36] and Amitay and Glezer [37] which observed that locating the actuator near the boundary layer separation point, a lower momentum coefficient was needed to reattach the separated flow. Furthermore, Feero et al. [38] observed that the required C_μ to reattach the boundary layer was the lowest for excitation frequencies in the range of the vortex shedding frequency. The same observation was made by Tuck and Soria [39] then they reported optimal actuation frequencies of $F^+ = 0.7$ and 1.3, the highest one being most effective in combination with an optimum momentum coefficient of $C_\mu = 0.0123$. Kitsios et al. [40] conducted a LES study on a NACA-0015 airfoil at $Re = 8.96 \times 10^5$ and noticed that the optimal pulsating frequency coincided with the baseline shedding frequency (f_{wake}). This was also experimentally confirmed by Buchmann et al. [41] and corroborated using (3D-DNS) by Zhang and Samtaney [42]. Numerical studies on the NACA-23012 airfoil at $Re = 2.19 \times 10^6$ were performed by [43,44] and concluded that maximum lift was obtained when $F^+ = 1$, the jet was placed nearby the boundary layer separation point, and tangential injection/suction was observed to be particularly effective.

The numerical work performed in the present manuscript describes a novel methodology based on parametric analysis optimization to maximize the aerodynamic efficiency of a given airfoil section. The method is applied to an airfoil section belonging to the DTU10MW Horizontal Axis Wind Turbine (HAWT). By considering the methodology here outlined and extending it to all Wind Turbine (WT) airfoil sections where the boundary layer is separated, the energy required to attach the boundary layer in all WT sections shall be minimized, therefore maximizing the energy increase obtained by any WT. It is particularly interesting to highlight that the attachment of the boundary layer along the blade span not only increases the aerodynamic efficiency of the blade and the wind turbine power but also decreases the downstream wake generated by the wind turbine. Many recent studies [45–47] are analyzing the power loss suffered by wind turbines placed in wind farms due to the wake generated by turbines located upstream; therefore, the wind turbine wake reduction proposed in the present research may lead to a decrease of the distance consecutive wind turbines can be located in wind farms as well as a power increase of wind turbines placed downstream.

The remainder of the paper is structured as follows: The problem formulation, numerical methods, and mesh independence study are presented in Section 2. Section 3 serves to define the WT's main characteristics and the airfoils selected to be simulated via CFD. The baseline case study of the different sections, the complete parametric analysis of the chosen airfoil, and the energy assessment are to be found in Section 4. The research performed is summarized in Section 5.

2. Numerical Method

2.1. Governing Equations and Turbulence Model

The Navier–Stokes (NS) equations under incompressible flow conditions take the following form:

$$\frac{\partial u_i}{\partial x_i} = 0 \tag{1}$$

$$\frac{\partial u_i}{\partial t} + \frac{\partial u_i u_j}{\partial x_j} = -\frac{1}{\rho}\frac{\partial p}{\partial x_i} + \nu \frac{\partial^2 u_i}{\partial x_j \partial x_j} \tag{2}$$

As Reynolds number increases, the mesh and the associated time step NS equations require drastic decreases in order to reach the Kolmogorov length and time scales, but reaching such scales involves extremely large computational times; such simulations are called Direct Numerical Simulations (DNS). Due to its drawbacks, nowadays DNS is just used for research purposes and for relatively small Reynolds numbers. For highly turbulent

flow and to obtain reasonably accurate results, turbulence models are still needed. The use of Large Eddy simulation (LES) as a turbulence model is a very good option in 3D flows, yet it still requires very fine meshes and large computational times; therefore, LES simulations require supercomputers to shorten the computational time. As a result, simulations at large Reynolds numbers still need to be performed using Reynolds Averaged Navier Stokes (RANS) or URANS unsteady-RANS turbulence models. Their precision is not as accurate as LES or DNS, but the computational time needed shortens drastically.

Under incompressible flow conditions, the only variables associated with the NS equations are the pressure and the three velocity components, which are generically called ϕ. In order to be able to apply URANS models, each variable from the NS equations needs to be substituted by its average $\bar{\phi}$ and a fluctuation ϕ' term.

$$\phi = \bar{\phi} + \phi' \tag{3}$$

After the substitution, the resulting NS equations (considering just two dimensions) take the following form:

$$\frac{\partial \bar{u}_x}{\partial x} + \frac{\partial \bar{u}_y}{\partial y} = 0 \tag{4}$$

$$\frac{\partial \bar{u}_x}{\partial t} + \bar{u}_x \frac{\partial \bar{u}_x}{\partial x} + \bar{u}_y \frac{\partial \bar{u}_x}{\partial y} = -\frac{1}{\rho}\frac{\partial p}{\partial x} + g_x + \frac{1}{\rho}\frac{\partial}{\partial x}\left(2\mu \frac{\partial \bar{u}_x}{\partial x} - \rho(\bar{u}_x')^2\right) + \frac{1}{\rho}\frac{\partial}{\partial y}\left(\mu\left(\frac{\partial \bar{u}_x}{\partial y} + \frac{\partial \bar{u}_y}{\partial x}\right) - \rho\overline{u_x' u_y'}\right) \tag{5}$$

$$\frac{\partial \bar{u}_y}{\partial t} + \bar{u}_x \frac{\partial \bar{u}_y}{\partial x} + \bar{u}_y \frac{\partial \bar{u}_y}{\partial y} = -\frac{1}{\rho}\frac{\partial p}{\partial y} + g_y + \frac{1}{\rho}\frac{\partial}{\partial x}\left(\mu\left(\frac{\partial \bar{u}_y}{\partial x} + \frac{\partial \bar{u}_x}{\partial y}\right) - \rho\overline{u_y' u_x'}\right) + \frac{1}{\rho}\frac{\partial}{\partial y}\left(2\mu \frac{\partial \bar{u}_y}{\partial y} - \rho(\bar{u}_y')^2\right) \tag{6}$$

It is now relevant to consider the concept of the apparent Reynolds stress tensor (τ_{app}), which comprises a symmetric matrix encompassing the time-averaged fluctuations in the x, y, and z directions. It is important to observe that in the case of two-dimensional flows, this matrix explicitly consists of four terms, whereas in three dimensions, it expands to a 3×3 symmetric matrix.

Some RANS turbulence models are based on solving the Navier–Stokes equations by incorporating the concept of turbulence viscosity (μ_t), which can be mathematically implemented into the momentum equations described above using the subsequent definition (called the Boussinesq hypothesis):

$$\mu_t = \frac{-\rho\overline{u_x' u_x'}}{2\dfrac{\partial \bar{u}_x}{\partial x}} = \frac{-\rho\overline{u_y' u_y'}}{2\dfrac{\partial \bar{u}_y}{\partial y}} = \frac{-\rho\overline{u_x' u_y'}}{\dfrac{\partial \bar{u}_x}{\partial y} + \dfrac{\partial \bar{u}_y}{\partial x}} \tag{7}$$

The X and Y momentum terms of the NS equations can therefore be expressed as follows:

$$\frac{\partial \bar{u}_x}{\partial t} + \bar{u}_x \frac{\partial \bar{u}_x}{\partial x} + \bar{u}_y \frac{\partial \bar{u}_x}{\partial y} = g_x - \frac{1}{\rho}\frac{\partial p}{\partial x} + \frac{1}{\rho}\frac{\partial}{\partial x}\left(2(\mu + \mu_t)\frac{\partial \bar{u}_x}{\partial x}\right) + \frac{1}{\rho}\frac{\partial}{\partial y}\left((\mu + \mu_t)\left(\frac{\partial \bar{u}_x}{\partial y} + \frac{\partial \bar{u}_y}{\partial x}\right)\right) \tag{8}$$

$$\frac{\partial \bar{u}_y}{\partial t} + \bar{u}_x \frac{\partial \bar{u}_y}{\partial x} + \bar{u}_y \frac{\partial \bar{u}_y}{\partial y} = g_y - \frac{1}{\rho}\frac{\partial p}{\partial y} + \frac{1}{\rho}\frac{\partial}{\partial x}\left((\mu + \mu_t)\left(\frac{\partial \bar{u}_x}{\partial y} + \frac{\partial \bar{u}_y}{\partial x}\right)\right) + \frac{1}{\rho}\frac{\partial}{\partial y}\left(2(\mu + \mu_t)\frac{\partial \bar{u}_y}{\partial y}\right) \tag{9}$$

We have chosen to use the k-ω SST turbulence model, which relies on using the k-ω model near the wall, the k-ϵ model far away from the object, and a blending function between these two. Mathematically, μ_t is calculated as follows:

$$\mu_t = \frac{\rho k}{\omega} \quad \longrightarrow \quad \begin{cases} \rho : \text{density} \\ k : \text{turbulent kinetic energy} \\ \omega : \text{turbulent kinetic energy specific dissipation rate} \end{cases} \tag{10}$$

As stated, this model is a two-transport equation model in order to solve k and ω. The transport equations used to define each parameter are as follows:

$$\frac{\mathrm{D}(\rho k)}{\mathrm{D}t} = \tau_{ij}\frac{\partial u_i}{\partial x_j} - \beta^*\rho k\omega + \frac{\partial}{\partial x_j}\left[(\mu + \sigma_k\mu_t)\frac{\partial k}{\partial x_j}\right] \tag{11}$$

$$\frac{\mathrm{D}(\rho\omega)}{\mathrm{D}t} = \frac{\gamma}{\nu_t}\,\tau_{ij}\frac{\partial u_i}{\partial x_j} - \beta\rho\omega^2 + \frac{\partial}{\partial x_j}\left[(\mu + \sigma_\omega\mu_t)\frac{\partial \omega}{\partial x_j}\right] + 2\rho(1-F_1)\sigma_{\omega 2}\frac{1}{\omega}\frac{\partial k}{\partial x_j}\frac{\partial \omega}{\partial x_j}, \tag{12}$$

where the turbulent stress tensor τ_{ij} is defined as

$$\tau_{ij} = \mu_t\left(\frac{\partial u_i}{\partial x_j} + \frac{\partial u_j}{\partial x_i} - \frac{2}{3}\frac{\partial u_k}{\partial x_k}\delta_{ij}\right) - \frac{2}{3}\rho k\delta_{ij} \tag{13}$$

The SST model combines the constants of the k-ω and k-ϵ turbulence models, defined as ϕ_1 and ϕ_2, respectively, using a blending function F_1, which depends on the distance of the first cell to the wall. The generic values taken by the different constants ϕ are blended as follows:

$$\phi = F_1\phi_1 + (1 - F_1)\phi_2, \tag{14}$$

where F_1 is the blending function defined as

$$F_1 = \tanh\left((\arg 1)^4\right), \tag{15}$$

being the argument arg1 given by

$$\arg 1 = \min\left(\max\left(\frac{\sqrt{k}}{0.09\omega y}, \frac{500\nu}{y^2\omega}\right), \frac{4\rho\sigma_{\omega 2}k}{CD_{k\omega}y^2}\right). \tag{16}$$

The constants ϕ_1 and ϕ_2 employed by the corresponding turbulent model are having the following values: $\sigma_{k1} = 0.85$, $\sigma_{\omega 1} = 0.5$, $\beta_1 = 0.075$,$\beta^* = 0.09$, $\kappa = 0.41$, $\gamma_1 = \frac{\beta_1}{\beta^*} - \sigma_{\omega 1}\kappa^2/\sqrt{\beta^*}$. $\sigma_{k2} = 1.0$, $\sigma_{\omega 2} = 0.856$, $\beta_2 = 0.0828$, $\gamma_2 = \frac{\beta_2}{\beta^*} - \sigma_{\omega 2}\kappa^2/\sqrt{\beta^*}$. For an in-depth understanding of the proposed k-ω SST turbulence model, the reader should refer to [48,49].

2.2. Non-Dimensional Parameters

Reynolds Number

The Reynolds number is defined as the ratio of inertial to viscous forces. Mathematically, it is expressed as follows:

$$Re = \frac{\rho u_{rel} C}{\mu} \tag{17}$$

where u_{rel} is the relative velocity, C the chord length, and μ the fluid absolute viscosity.

Aerodynamic Coefficients

The most common aerodynamic coefficients are the lift C_l and drag C_d ones, which are mathematically expressed as follows:

$$C_l = \frac{L}{\frac{1}{2}\rho u_{rel}^2 C} \qquad C_d = \frac{D}{\frac{1}{2}\rho u_{rel}^2 C} \tag{18}$$

L and D represent the lift and drag forces, respectively.

The aerodynamic efficiency is the ratio between the lift and drag coefficients:

$$\eta = \frac{C_l}{C_d} \tag{19}$$

Pressure Coefficient

It characterizes the relative pressure field ($p - p_\infty$) along the body.

It is mathematically expressed as

$$C_p = \frac{p - p_\infty}{\frac{1}{2}\rho u_{rel}^2} \tag{20}$$

where $((1/2)\rho u_{rel}^2)$ is defined as the dynamic pressure.

Friction Coefficient

The friction coefficient, also known as the skin friction coefficient or tangential friction coefficient, evaluates the frictional force per unit area τ_w acting on a surface in contact with the fluid.

$$C_f = \frac{\tau_w}{\frac{1}{2}\rho u_{rel}^2} \tag{21}$$

Momentum Coefficient

It represents the momentum associated with the jet divided by the incoming fluid momentum. According to reference [34], C_μ is the primary AFC parameter. Mathematically it is expressed as follows:

$$C_\mu = \frac{h\left(\rho u_{max}^2\right) \sin\theta_{\text{jet}}}{C\left(\rho u_{rel}^2\right)} \tag{22}$$

where (h) is the jet width, (u_{max}) is the maximum jet velocity, and (θ_{jet}) is the jet inclination angle with respect to the airfoil surface.

Forcing Frequency

The forcing frequency, given as a non-dimensional number, is defined as follows:

$$F^+ = \frac{f}{f_0} \tag{23}$$

where f is an arbitrary frequency and f_0 is the vortex shedding frequency (the frequency at which vortices are shed from the airfoil).

Courant–Friedrichs–Levy Number

The Courant number, often denoted as CFL, quantifies how the numerical scheme/setting correctly captures the propagation of the information in the flow due to its velocity. Mathematically, it is defined as the fluid velocity measured at any given mesh cell multiplied by the simulation time step and divided by the mesh cell length scale (Δx).

$$CFL = \frac{u\Delta t}{\Delta x} \tag{24}$$

For time-dependent simulations, the Courant number is an important parameter in order to ensure the stability of the system, and it is recommended to keep it below 1.

Dimensionless Wall Distance

The dimensionless wall distance y^+ represents the distance from the wall to the first mesh cell, y, normalized by a characteristic velocity u_τ and the relative viscosity of the fluid ν. Mathematically, it is expressed as follows:

$$y^+ = \frac{u_\tau y}{\nu} \tag{25}$$

where u_τ is the friction velocity, defined as

$$u_\tau = \sqrt{\frac{\tau_w}{\rho}} \tag{26}$$

2.3. Numerical Domain and Boundary Conditions

For computational domains relatively small in respect to the bluff-body characteristic length, the flow around the bluff-body is affected by the boundary conditions defined at the boundaries. Conversely, if the domain is chosen to be too large, there may be excessive mesh cells, resulting in longer computational times and poor simulation efficiency. Therefore, it is crucial to choose an appropriate domain size that balances the need for accurate results with computational efficiency.

Based on the previous research undertaken by [22,24,50], the computational domain employed in the present research has the following dimensions: 10C from the domain inlet to the airfoil leading edge, 15C from the trailing edge to the domain outlet, and 10C from the body surface to both the upper and lower limits of the domain, C being the airfoil chord; see Figure 1.

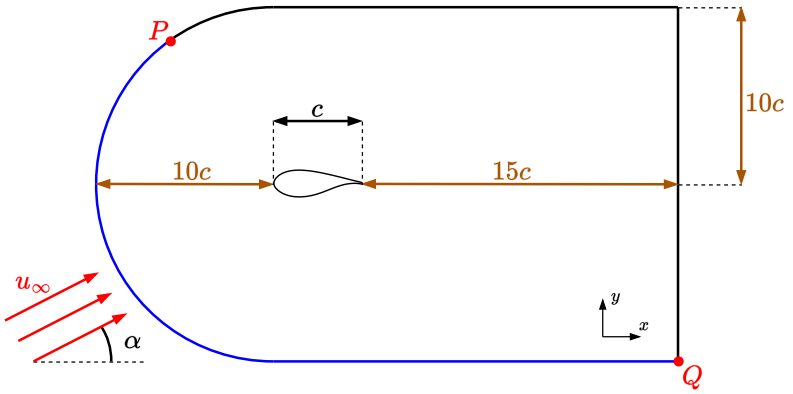


Figure 1. Schematic view of the meshing domain within its general dimensions.

Two points, P and Q, delimiting the inlet and outlet boundaries, have been implemented in Figure 1. The outlet boundary extends from P to Q in a clockwise direction, and from P to Q in a counterclockwise direction is to be found the inlet boundary. The curvilinear shape of the domain at the inlet has been selected to facilitate the simulation of various angles of attack without altering the mesh geometry. It should be noted that the airfoil has been horizontally positioned, and by adjusting the inlet velocity components, any required angle of attack can be obtained. This approach not only allows flexibility in the simulation but also ensures that the mesh remains consistent throughout the analysis.

The present research focuses on simulating external aerodynamics with transient turbulent flow (aerodynamic forces change over time) and at large Reynolds numbers of the order of $\mathcal{O}(10^7)$. Additionally, the angle of attack is relatively high for the two baseline case sections studied, which, particularly for the section placed nearest the blade root (Section 54 of the DTU-10MW-HAWT), is expected to produce the separation of the boundary layer at some point along the chord, generating the corresponding vortical structures and vortex shedding. Moreover, since the relative velocity in both sections studied does not exceed the incompressible flow limit, which is commonly accepted as $M < 0.3$, the flow will be considered as incompressible across the entire study. The flow solver contained in the OpenFOAM package, which fulfills the needs for the present research, is *PisoFoam* (Pressure implicit with splitting operator). This solver is particularly well suited for simulating unsteady turbulent flow and is widely used in aerodynamic simulations due to its accuracy and efficiency.

Section 54 with a wind speed of 10 m/s was chosen to perform the mesh independence study. Notice that the Reynolds number is almost the same in both sections, and the angle of attack is much larger in this particular one. The main data relative to the two sections studied, Sections 54 and 81, are presented in Table 1, which includes the airfoil type, the radius versus the turbine main axis, the section number, the chord length, the Reynolds number, the angle of attack, and the relative velocity, which is the vectorial magnitude

obtained from the combination of the wind and turning speeds and when considering the axial (a) and angular (a′) induction factors. Figure 2 introduces the approximate location of the two sections under study as well as their respective profile.

Table 1. Main characteristics of the two sections studied (Sections 54 and 81).

Airfoil Type	FFA-W3-301	FFA-W3-301
Radius (z)	31.42 m	53.43 m
Section Number (N)	54	81
Chord length (c)	6.06 m	4.44 m
Reynolds number (Re)	14.08×10^6	14.87×10^6
Angle of Attack (α)	17.79 deg.	10.01 deg.
Free-stream velocity (u_{rel})	34.40 m/s	49.61 m/s

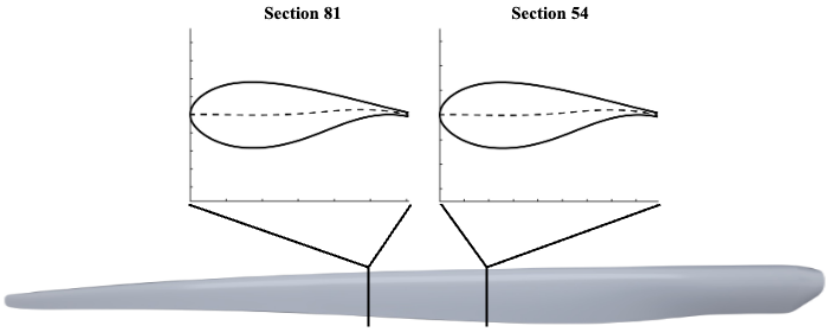


Figure 2. Three-dimensional view of the DTU10MW blade with the two sections studied.

The different boundary conditions employed to simulate section 54, regardless of the mesh density considered, are outlined in Table 2. It's worth noting that these specific values are based on the k-ω SST turbulence model, aligned with the corresponding chord length and a turbulence intensity at the inlet of 0.1 % and according to [48,49]. In this paper, all simulations were performed using air at sea level based on the International Standard Atmosphere (ISA). The two relevant air parameters, density and kinematic viscosity, are summarized in Table 3.

Table 2. Summary of the boundary conditions for the baseline case. Section 54 at $u_\infty = 10$ m/s. The different parameters represent the turbulence kinetic energy k (m^2/s^2), the turbulence specific dissipation rate ω (s^{-1}), the turbulence kinematic viscosity ν_t (m^2/s), the pressure P (Pa), and the incoming fluid relative velocity u_{rel} (m/s).

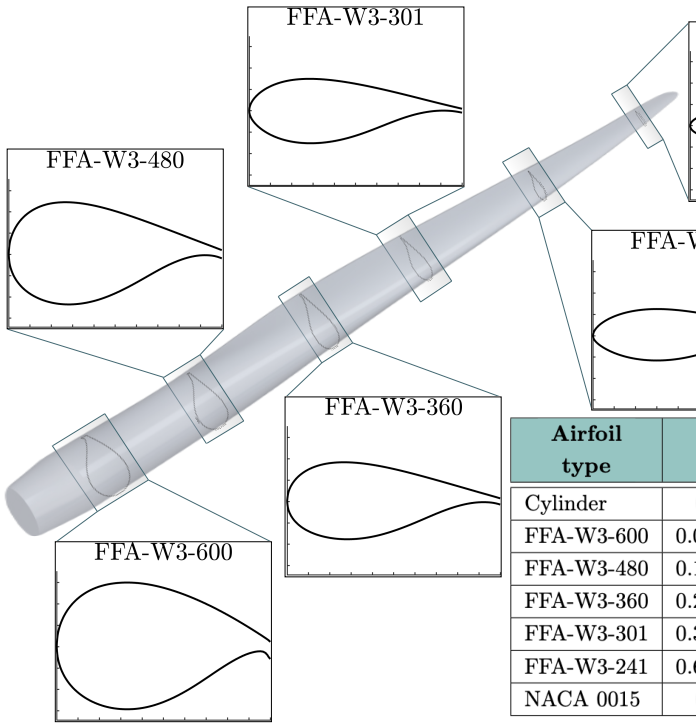
	Simulation Parameters				
	k (m^2/s^2)	ω (s^{-1})	ν_t (m^2/s)	$P(Pa)$	u_{rel} (m/s)
Inlet	1.78×10^{-3}	6.95×10^{-3}	2.25×10^{-1}	zeroGrad.	$u_x = 32.75$; $u_y = 10.51$
Outlet	zeroGrad.	zeroGradient	zeroGradient	0	zeroGrad.
Front and back	empty	empty	empty	empty	empty
Wall	10^{-20}	ohmegaWallFunc. value 10^{-5}	nutLowReyWallFunct. value 0	zeroGrad.	0

Table 3. Density and kinematic viscosity values at sea level and according to ISA conditions.

Density (ρ)	1.225 kg/m^3
Kinematic Viscosity (ν)	1.48×10^{-5} m^2/s

2.4. Mesh Assessment

The blade considered in the present research is the DTU-10MW offshore HAWT and consists of six different airfoil types, which, seen from the central axis to the blade tip, see Figure 3, are FFA-W3-600; FFA-W3-480; FFA-W3-360; FFA-W3-301; FFA-W3-241; and NACA0015. Note that DTU implemented a Gurney flap at the trailing edge of the FFA-W3-600 airfoil type, so in terms of meshing, this modification must be considered. The mesh independence study was performed using Section 54, which belongs to the FFA-W3-301 airfoil type. For a wind speed of 10 m/s, the Reynolds number associated with this section is $Re = 14.08 \times 10^6$, and considering the angle of attack associated, boundary layer separation is expected to occur.



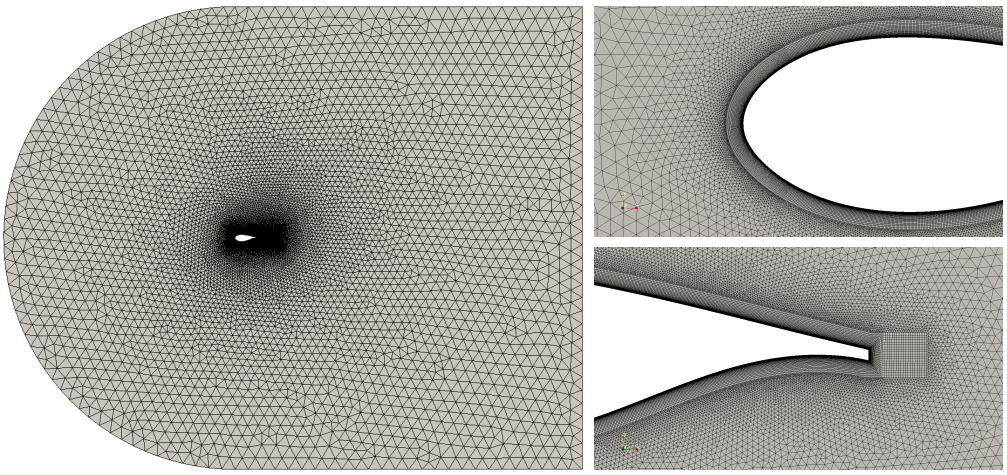
Airfoil type	z/R [-]	z [m]
Cylinder	0 – 0.050	0 – 4.458
FFA-W3-600	0.050 – 0.160	4.458 – 14.267
FFA-W3-480	0.160 – 0.250	14.267 – 22.292
FFA-W3-360	0.250 – 0.340	22.292 – 30.316
FFA-W3-301	0.340 – 0.600	30.316 – 53.500
FFA-W3-241	0.600 – 0.990	53.500 – 88.274
NACA 0015	0.990 – 1	88.274 – 89.166

Figure 3. Blade diagram with the different airfoil profiles along the blade span.

For the FFA-W3-301 airfoil family, a C-type body-fitted structured mesh has been chosen for the region close to the airfoil. The C-type mesh comprises a curvilinear line surrounding the solid geometry, which is closed on the leading edge of the airfoil but open on the trailing edge. The region between the airfoil and the C-line is where the structured mesh is allocated; this region is usually called the "halo." The halo thickness employed in the present research and measured perpendicular to the airfoil surface is about 3.2% of the chord; this value was kept constant for the two airfoils considered. A general view of the computational domain with the hybrid mesh employed is presented in Figure 4a. A zoomed view of the structured mesh zones at the airfoil's leading and trailing edges is presented in Figure 4b, where the details of the mesh at the trailing edge are observed. A small, rectangularly structured domain has been employed at the trailing edge region to properly capture the vortical structures due to possible flow detachment. The remaining portion of the computational domain has been designated with a non-structured mesh; see Figure 4a. This choice is rooted in the understanding that a certain level of reduced accuracy in regions distant from the airfoil surface is acceptable. Furthermore, opting for a hybrid mesh enables a more favorable balance between computational efficiency and accuracy of the results. Notwithstanding this, a heightened cell density has been strategically implemented in the vicinity of the airfoil to attain the desired level of precision.

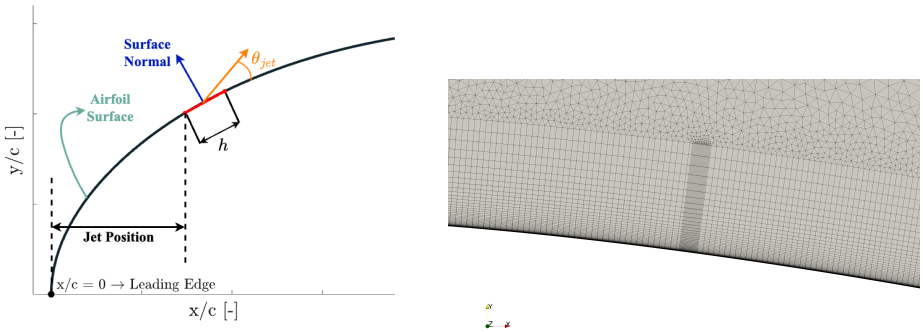
The implementation of the AFC technology using synthetic jets (SJ) requires the modification of the mesh in the location where the SJ is to be implemented. Figure 5b

presents a zoom view of the mesh around the SJ, and Figure 5a introduces the main SJ-associated parameters that will be tuned via the corresponding parametric optimization.



(**a**) Overall view (**b**) Zoomed views

Figure 4. Full view of the mesh in the computational domain (**a**), zoomed view of the structured mesh in the leading ((**b**) **top**) and trailing ((**b**) **bottom**) edges for FFA-W3-301 airfoil type.



(**a**) (**b**)

Figure 5. Synthetic jet position and associated parameters (**a**). Detailed view of the AFC mesh implementation in Section 54. (**b**)

To ensure maximum accuracy in the simulated results, a thorough investigation of the mesh density is required, particularly in the halo region near the airfoil surface where the boundary layer develops and it is likely to separate. In this region, a drastic velocity and shear stress evolution in the normal direction to the airfoil surface is to be expected. Due to the lack of prior experimental investigations considering the Reynolds number and the airfoil type chosen and noting that the previous numerical investigations performed by reference [51] presented the time-averaged value for C_l and C_d, a mesh independence study was performed to ensure a dissociation between mesh resolution and the outcomes produced, thus establishing a robust foundation for further analysis. The assessment for mesh independence involves generating four distinct meshes, all sharing identical overall geometries (depicted in Figure 4a), while varying the targeted y^+ values. For the purpose of result validation, the approach chosen involves examining the time-averaged C_l and C_d, as well as the distributions of C_p and C_f along the chord for each mesh resolution. This comparative study seeks to identify the y^+ value at which substantial result deviations are absent.

The simulations carried out encompassed a 28 s duration, wherein the average lift and drag coefficients were derived from a sampling window spanning the concluding 8 s of the simulation. The numerical outcomes of the averaged aerodynamic coefficients, coupled with the corresponding relative error denoted as ErrorC_l in percentage and versus the value obtained by [51], are presented comprehensively in Table 4. The number of cells used for each mesh, the minimum and maximum $y+$ at the airfoil surface, the airfoil efficiency η, as well as the boundary layer separation point denoted as x_s/C, are presented in the same table. Upon careful examination, it becomes evident that as the maximum y^+ is reduced, the error in the lift coefficient drastically drops, becoming negligible between the two finest meshes. For instance, the discrepancy stands at 4.45% between the C_l obtained for maximum $y^+ = 4.29$ and the value obtained by [51]; such discrepancy is reduced to 2.51% when comparing the reference value and the one obtained in meshes C and D. It is relevant to note that meshes C and D generate identical results for C_l and for the boundary layer separation x_s/C, and minor discrepancies are observed in the C_d values generated by these two meshes. A discrepancy of around 32% is observed when comparing the reference C_d with the one obtained in mesh C; this large discrepancy is understood when noting that the airfoil chord used in reference [51] was the unity, the Reynolds number being $Re = 10^7$. In the present study, the chord associated with Section 54 is 6.2 m, and the Reynolds number is 12.7×10^6, therefore clarifying why the drag coefficient, is a bit larger in the present study. Considering the notable accuracy achieved by Mesh C and the manageable computational time entailed in its simulation, it has been judiciously chosen as the preferred candidate for subsequent simulations.

Table 4. Time-averaged aerodynamic coefficients for different meshes at wind speed = 10 [m/s]. The different columns respectively represent the mesh name, the number of cells of the respective mesh, the minimum and maximum y+ values, the lift coefficient, the error versus the one obtained by [51], the drag coefficient, and the aerodynamic efficiency.

Mesh	N_{cell}	**Min** y^+	**Max** y^+	x_s/C	C_l	C_l **Error [%]**	C_d	$\eta(C_l/C_d)$
A	100K	0.513	4.29	0.39	1.5312	4.45	0.11975	12.79
B	172K	0.169	0.98	0.41	1.5408	3.85	0.11881	13.04
C	191K	0.064	0.71	0.42	1.5623	2.51	0.10625	14.71
D	215K	0.039	0.49	0.42	1.5623	2.51	0.09985	15.64
[51]					1.6025	-	0.08	20.03

For a visual and perhaps more precise comparison of the outcomes, an illustrative representation has been generated to showcase the variation in pressure and friction coefficients across the chord length and for the four distinct tested meshes, as exhibited in Figure 6a,b. Examining the pressure distribution over both the upper and lower surfaces of the airfoil reveals a remarkably uniform behavior across all the meshes. Notably, there exists a consistent and gradual pressure recovery on the upper surface. The sole discernible divergence in pressure coefficients among all the meshes manifests near the 1.5 m $= x/C = 0.24$ mark along the chord. Nevertheless, the graph depicting C_p presents a strikingly analogous pattern for all the meshes. In the realm of the friction coefficient graph, as depicted in Figure 6b, distinctions emerge among the meshes. Notably, the lower y^+ meshes, namely Mesh A and B, exhibit some variations in the boundary layer separation point, x_s/C. Conversely, Mesh C closely mirrors the C_f trends observed in Mesh D, aligning with the minor errors observed in the averaged aerodynamic coefficients. This alignment renders Mesh C the optimal selection for future simulations.

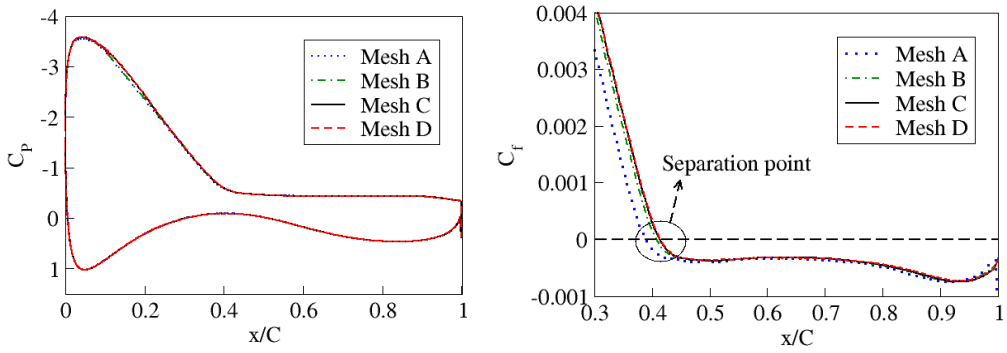


Figure 6. Pressure (**a**) and friction (**b**) coefficients comparison for the four meshes evaluated in Section 54.

3. Main Parameters Definition of the DTU 10MW RWT

In order to increase the accuracy of the 2D-CFD simulations, it is important to consider the flow's three-dimensional effects over the airfoil section under study. Two induction factors, axial (a) and tangential (angular) (a'), which consider some flow three-dimensional effects, are used to more precisely calculate the axial and radial velocities for 2D simulations [52]. The decrease in streamwise velocity from the free-stream conditions to the rotor plane is called the axial velocity deficit, and the fraction by which it is reduced is called the axial induction factor (a). The tangential induction factor (a')considers the increase of the tangential speed in the rotor plane. Figure 7 introduces the typical velocity and force components acting on a generic HAWT airfoil, and considering the corresponding induction factors, the main angles associated are also depicted. The aerodynamic forces (lift and drag) are decomposed into radial and tangential directions. For the present study, the values of the induction factors corresponding to each of the two airfoil sections studied, Sections 54 and 81, were obtained from [53].

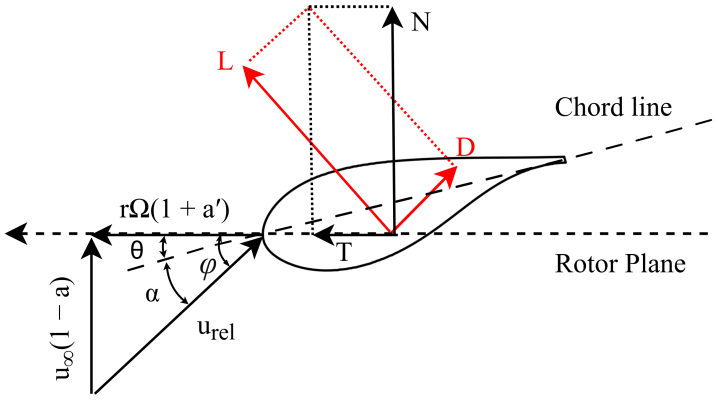


Figure 7. Wind, rotor velocities, and forces on a generic blade section.

Additionally, for the computation of essential metrics such as net force, torque, angle of attack, and relative wind speed for each blade section, as described by Formulas (27)–(30) from [54,55], the framework necessitates the establishment of two distinct angles. These angles serve as pivotal factors in the analytical processes. The initial angle, referred to as θ, corresponds to the angle formed between the section chord and the plane of rotation, designated as the section twist angle. This angle, which is different for each section, is defined in the design process of each HAWT and cannot be modified. In fact, and in order to obtain the maximum power for each given wind speed, HAWT traditionally uses the blade pitch angle, not depicted in Figure 7; note that the pitch angle is constant for all blade sections and just depends on the wind speed. For the present DTU10MW RWT,

when the wind speed is 10 m/s, the pitch angle is zero. Lastly, the other angle that plays a crucial role in the calculations is labeled as φ and characterizes the inflow angle. This angle quantifies the divergence between the relative wind speed of each blade section and the plane of rotation, as delineated in Figure 7. Notice that the angle of attack (AoA) is given as $\alpha = \varphi - \theta$.

Based on the information just presented, the relation between the relative velocity u_{rel}, the free stream velocity u_∞, and the tangential one Ωr, r being the section (airfoil) radius and Ω standing for the wind turbine turning speed, is given as Equation (27).

$$u_{rel} = \sqrt{(\Omega r(1+a'))^2 + (u_\infty(1-a))^2} \tag{27}$$

The equation defining the angle of attack (given in degrees) for any blade section takes the following form:

$$\alpha = \arctan\left(\frac{u_{rel}(1-a)}{\Omega r(1+a')}\right) \cdot \frac{360}{2\pi} - \theta \tag{28}$$

For a given section, the resultant force acting on the rotor plane direction (T) and the force acting in a plane perpendicular to it (N), are expressed as.

$$T = \frac{1}{2} C \rho u_{rel}^2 (C_l \sin\varphi - C_d \cos\varphi) \tag{29}$$

$$N = \frac{1}{2} C \rho u_{rel}^2 (C_l \cos\varphi + C_d \sin\varphi) \tag{30}$$

From Equation (29), several insights can be derived regarding the significance of lift and efficiency across different parts of the blade: when dealing with high inflow angles at the root region (close to 90 deg.), the contribution of the lift coefficient becomes more significant than that of drag in torque generation. Conversely, at the tip, the drag coefficient (and hence the aerodynamic efficiency) plays a more prominent role, making it crucial to enhance efficiency in this region. Based on the Angles of Attack (AoA) associated with each section and the aerodynamic data provided by reference [56], it is estimated that approximately 40% of airfoils will experience separated flow at a wind speed of 10 m/s, making it a good regime for enhancing the aerodynamic capabilities via AFC implementation. It should be noted that other wind velocities also have a high number of airfoils in post-stall conditions, which opens a door into improving the WT efficiency and power generated.

4. Results

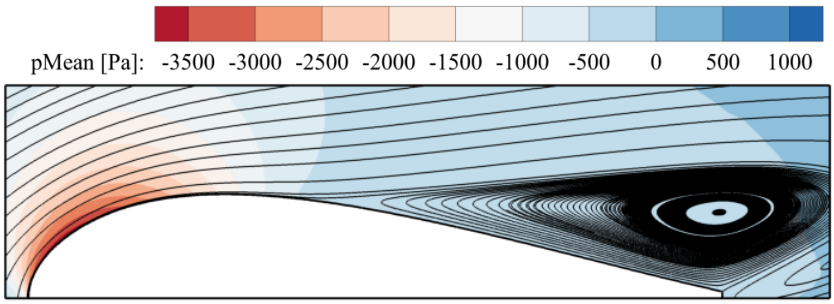
4.1. Baseline Case Results Summary

Delving into the results of the baseline case simulations, it will initially present the numerical values encompassing the time-averaged lift C_l and drag C_d coefficients, the peak-to-peak (PTP) variations of the parameters PTP_{C_l} and PTP_{C_d}, the aerodynamic efficiency η, the non-dimensional boundary layer separation points x_{sep}/C, and the dimensional vortex shedding frequencies f_0. For the specific numerical values already mentioned, the reader should refer to Table 5, where the comparison of the lift and drag coefficients obtained from previous research work [51,53] is also presented.

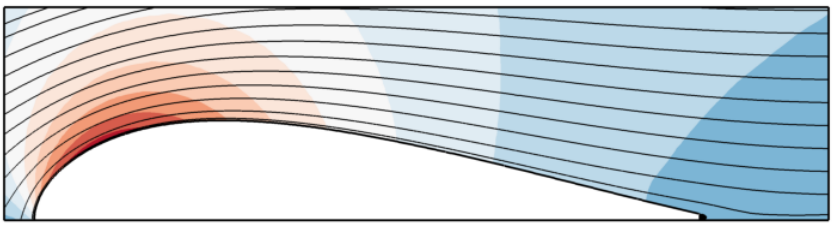
From the data presented in this table, several key insights can be gleaned about the behavior of the blade's middle sections at moderate wind speeds. It becomes evident that they share common traits such as a heightened lift-to-drag ratio and rather small peak-to-peak oscillation magnitudes. Furthermore, it is noteworthy that the oscillation frequencies remain relatively subdued for Section 54, whereas for Section 81, and due to the fact that there is no boundary layer separation, small vortical structures are just appearing at the airfoil trailing edge, the oscillations occur at a much more rapid rate. The comparison of the lift coefficient of Sections 54 and 81 with previous reference values shows errors of 7.5% and 1.6% versus the ones given in reference [53]; respectively, such C_l discrepancies are of 2.5% and 16% when compared with the respective values obtained in [51]. As already

presented in Table 4, the C_d error versus the present Section 54 and the results from [51] is of around 32%, this error being of 330% when compared with [53]. The already reported differences in chord length and Reynolds number between the present research and the one from [51] clarified the origin of the discrepancies. To understand the origin of the C_d discrepancies versus the 3D results presented by [53], it needs to be noted that in their research no boundary layer separation was observed in this particular section, probably due to the much coarser mesh they used; then their reported y+ was around 2, while it is around 0.7 in the present simulations. Note as well the large discrepancies in the lift and drag coefficient values presented in these two [51,53] references, therefore indicating that much more accurate simulations are needed to properly determine the boundary layer dynamics as well as the force coefficients; the present research is a small step in this direction.

In order to have an illustrative overview of the data presented in Table 5, Figure 8 provides the time-averaged of the streamlines at the upper surface of the two airfoils studied as well as the time-averaged of the pressure fields. The location where the fluid has a maximum acceleration, the area where time-averaged pressure is minimum, is almost the same for both sections. The vortical structures forming on top of Section 54 and its associated boundary layer separation point can now be clearly seen. The very small vortical structures having a frequency of around 28.8 Hz are not spotted from the view presented of Section 81. Yet this information is obtained from the Fast Fourier Transformation (FFT) of the dynamic lift signal.



(**a**) Section 54



(**b**) Section 81

Figure 8. Velocity fields given as time-averaged streamlines and time-averaged pressure fields for Sections 54 and 81.

Table 5. Summary of the main parameters of the baseline case simulations at a wind speed of 10 m/s. Including the averaged aerodynamic coefficients, the PTP values, the separation point, and the vortex shedding frequency.

Ref.	Section	C_l	C_d	$\eta = (C_l/C_d)$	PTP_{C_l}	PTP_{C_d}	x_{sep}/c	f_0(Hz)
Present		1.5623	0.10625	14.71	0.281	0.104	0.423	7.1
[51]	54	1.6025	0.08	20.03				
[53]		1.45273	0.02467	58.88				
Present		1.2097	0.0296	40.86	0.0038	0.0011	-	28.8
[51]	81	1.45	0.016	90.62				
[53]		1.23	0.014	87.85				

Delving into the post-processing graphs, Figure 9a,b present the pressure and friction coefficients comparison for the two sections studied, from where it is seen that a high lift coefficient is directly linked to a large pressure coefficient below the airfoil and a particularly low pressure coefficient on the airfoil upper surface. In Section 54, there is a pronounced suction peak on the upper surface near the leading edge, followed by a rapid pressure recovery and subsequently, a nearly constant value of C_p. This observation suggests a potential flow separation near that particular location. The friction coefficient becomes negative once the boundary layer is separated, and the pressure on the airfoil upper surface approaches the atmospheric one. The pressure coefficient distribution for Section 81 also includes a high suction peak at early chord coordinates followed by a smooth pressure recovery, which appears to point out that no flow separation is to be expected. The friction coefficient also shows a smooth decrease along the airfoil chord but does not become negative.

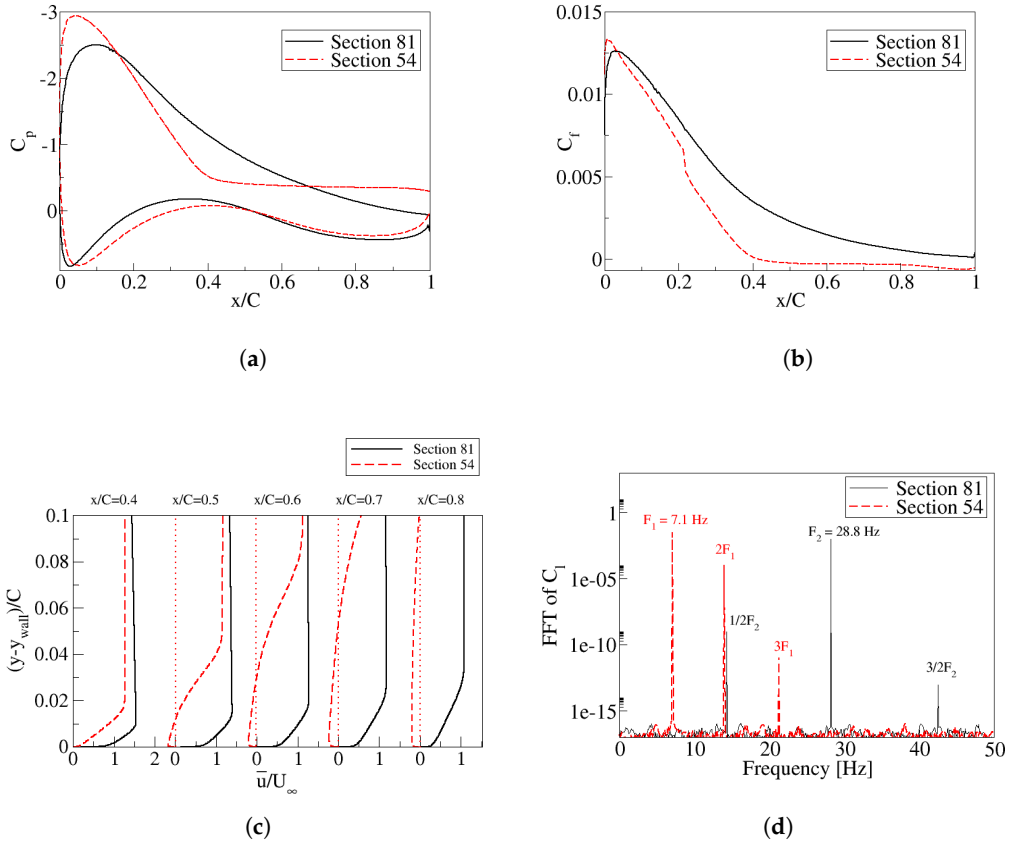


Figure 9. Post-processing results for Sections 54 and 81. Pressure coefficient distribution along upper and lower airfoil surfaces (**a**). Tangential friction coefficient distribution along airfoils upper surfaces (**b**). Mean velocity distribution tangent to the airfoils upper surfaces and as a function of the normalized wall normal distance (**c**). Fast Fourier Transform (FFT) of lift coefficients (**d**).

The velocity field tangent to the airfoil surface, as well as the FFT of the dynamic lift coefficient for both sections, are introduced in Figure 9c and 9d, respectively. As discussed previously, when the friction coefficient reaches a null value at a certain point along the airfoil surface, it indicates flow separation. This phenomenon is illustrated in Figure 9b, where the friction coefficient of Section 54 is observed to intersect the 0 value at an x coordinate of 2.566 m from the leading edge. In contrast, the C_f of Section 81 is not showing any x-axis crossing, indicating there is no flow separation. The boundary layer separation point is further seen in Figure 9c, where the velocity distribution tangential to the airfoil surface is shown along the chord; notice that the velocity field is already negative nearby the wall at a position $x/c = 0.5$ and further downstream, as previously observed

in Figure 9b. Finally, Figure 9d presents the vortex shedding frequency read from the lift coefficient. Notice that, as expected, when the boundary layer is separated, the vortex shedding frequency associated is much smaller, Section 54, than when the separation occurs at the airfoil trailing edge, Section 81.

4.2. Airfoil Section Chosen for the AFC Implementation

From the two sections analyzed, only Section 54 presents flow separation; this section is therefore chosen for AFC implementation via a parametric analysis. AFC is capable of reducing drag and increasing lift forces; its implementation shall generate a reduction in aerodynamic loads on the blade's downstream direction while increasing the torque generated.

The placement of the AFC groove is based on previous research works [35–37], where it was concluded that the optimum location for the groove was in the vicinity of the boundary layer separation point. Which for the chosen section occurs at $x = 2.566$ m, $x/C = 0.423$ (approximately 42 % of the airfoil's chord). As defined in Equation (22), the groove width is directly related to the jet momentum coefficient. For the present study, a width of $h = 0.5$ % of the airfoil chord was selected, a dimension widely accepted in the literature [23,24,50]. In the present parametric study, jet position and jet width were kept constant across the entire set of CFD simulations; therefore, the remaining three AFC parameters, momentum coefficient, jet inclination angle, and jet pulsating frequency, are the ones to be optimized. The parametric optimization employed consists of maintaining constant the jet inclination angle and jet pulsating frequency while changing the jet momentum coefficient until obtaining the maximum efficiency of the airfoil. The optimum value of the momentum coefficient, as well as the previous value of the jet frequency, will be kept constant on the second step of the process; different values of the jet inclination angle are evaluated until obtaining the one generating the maximum airfoil efficiency. On the final stage of the process, the changing variable will be the jet pulsating frequency.

To perform the parametric study, it is needed to modify the existing baseline mesh of Section 54, implementing a slot in the upper surface of the airfoil upwind of the separation point ($x/c = 0.4$), as depicted in Figure 5a. A zoomed view of the mesh implemented in the vicinity of the jet groove has been previously introduced in Figure 5b.

4.3. Momentum Coefficient C_μ Optimization

Synthetic jet actuators (SJA) generate zero net mass flux, which means that the mass flow through the AFC groove must be equal during both the suction and blowing phases. In order to achieve this statement, the time-dependent velocity profile for the AFC simulations is often chosen to be a sinusoidal trigonometric function, which is usually expressed as

$$u_{\text{jet}}(t) = u_{\max} \cdot \sin(2\pi f \cdot t) \tag{31}$$

where f is the synthetic jet actuation frequency, $u_{\max}$ is the maximum SJ outgoing/incoming velocity, and t is the time.

Based on previous studies [39–44], for optimum performance, the synthetic jet actuation frequency should be the same as or a multiple/submultiple of the vortex shedding one. This is why in our parametric analysis we will initially set the SJ pulsating frequency constant and equal to the vortex shedding one, which was $f_0 = 7.1$ Hz. The second parameter which will be initially kept constant is the jet inclination angle. A reasonable initial guess would be to inject the flow almost tangentially to the airfoil surface, taking advantage of the Coanda effect [57]. Thus, by injecting the pulsating flow tangentially to the airfoil surface, the Coanda effect can help to maintain the incoming flow attached to the airfoil. Based on several previous studies [22,23], we have decided to start the parametric analysis, maintaining a constant 10-degree SJ injection angle. At this point, four AFC parameters are initially set, and the parametric optimization starts via evaluating the effect of the momentum coefficient on the flow dynamics. The relation of the maximum velocity amplitude ($u_{\max}$) and the momentum coefficient can be extracted from (22). According to [43], relatively low momentum coefficients for AFC at high Reynolds numbers can lead

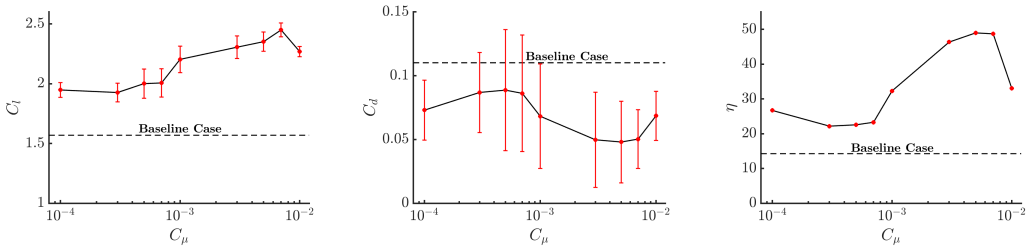
to improvements in the aerodynamic forces of airfoils. Kim and Kim [43] numerically investigated flow separation control with SJAs on a NACA23012 airfoil at $Re = 2.19 \times 10^6$, and they found that as momentum coefficient increased, lift improvement in comparison to the one obtained at small C_μ decreased. Moreover, to prevent reaching compressible flow effects on the groove exit, C_μ should be kept low. Therefore, momentum coefficients ranging between $C_\mu = 0.0001$ and $C_\mu = 0.01$ have been selected as an initial guess for the present application.

Table 6 presents a comprehensive overview of the AFC simulations for all C_μ evaluated as well as for the baseline case, offering numerical insights into the averaged lift and drag coefficients, aerodynamic efficiency, and peak-to-peak values for lift and drag coefficients. Notably, the data reveal that the momentum coefficient yielding the highest lift force is $C_\mu = 0.007$, the drag being particularly small under these conditions. Significantly, it is observed that there is a reduction in the amplitude of lift and drag coefficient oscillations when compared with the baseline case. It's worth noting that for the iterative process involving the momentum coefficient, this reduction isn't exceptionally pronounced; however, it can be deduced that, especially for high lift coefficients and low drag coefficients (i.e., high efficiencies), there is a slight decrease in the PTP values when compared with lower efficiency scenarios. In conclusion, it can be affirmed that delaying the boundary layer results in lift enhancement and drag reduction, accompanied by a dampening of the fluctuations of lift and drag forces.

Table 6. Time-averaged C_l, C_d, η and peak-to-peak PTP_{C_d}, PTP_{C_d} aerodynamic values obtained for the different C_μ considered. Jet inclination angle ($\theta_{\text{jet}} = 10$ deg.), forcing frequency ($F^+ = 1$), groove width $h = 0.005C$, and groove position $x/C = 0.4$. For comparison, the baseline case values are presented in the last row. (Red color indicated the optimum values).

C_μ	C_l	C_d	η	PTP_{C_l}	PTP_{C_d}
0.0001	1.947	0.073	26.678	0.122	0.047
0.0003	1.926	0.087	22.169	0.154	0.063
0.0005	2.000	0.089	22.550	0.244	0.095
0.0007	2.006	0.086	23.279	0.237	0.091
0.001	2.203	0.068	32.299	0.222	0.082
0.003	2.305	0.050	46.342	0.188	0.075
0.005	2.352	0.048	48.982	0.160	0.064
0.007	2.450	0.050	48.712	0.144	0.046
0.01	2.269	0.069	33.084	0.086	0.039
BCS S54	1.562	0.106	14.71	0.281	0.104

To gain further insight into the relationship between the lift coefficient and the momentum coefficient, Figure 10a is presented. The graph illustrates that at very low momentum coefficients, the jet fails to inject sufficient energy into the boundary layer, and the BL is likely to remain separated. As the momentum coefficient increases, the jet becomes more effective in energetically injecting air; a delay in the boundary layer separation is to be expected under these conditions. However, at excessively high momentum coefficients, where the jet velocity is very high, boundary layer tripping is likely to occur, and the boundary layer separation is promoted. The drag coefficient graph, Figure 10b, reveals a minimum value at $C_\mu = 0.005$, but it is followed by a slightly larger C_d value for $C_\mu = 0.007$. In terms of aerodynamic efficiency, Figure 10c demonstrates that the maximum efficiency is achieved at $C_\mu = 0.005$. This reinforces the selection of the momentum coefficient that yields maximum lift ($C_\mu = 0.007$), as it also exhibits a high efficiency, almost the same as the one obtained with $C_\mu = 0.005$. Note that the respective peak-to-peak values for C_l and C_d are also implemented in Figure 10. Note as well that all peak-to-peak amplitudes obtained for the lift and drag coefficients, regardless of the momentum coefficient considered, are smaller than the respective peak-to-peak amplitudes obtained in the baseline case simulations; see Table 6, clearly indicating a decrease of the dimension of the downstream vortical structures, which is linked with a delay of the boundary layer separation.



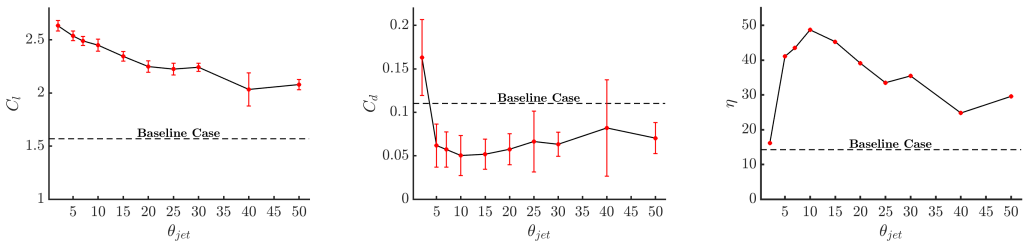
(**a**) (**b**) (**c**)

Figure 10. Lift coefficient (**a**), drag coefficient (**b**), and aerodynamic efficiency (**c**) variation as a function of momentum coefficient; the vertical bars characterize the corresponding peak-to-peak amplitude. Constant jet angle ($\theta_{\text{jet}} = 10$ deg.) and forcing frequency ($F^+ = 1$).

4.4. Jet Injection Angle Optimization

To optimize the jet inclination angle (θ_{jet}), the momentum coefficient obtained in the previous subsection ($C_\mu = 0.007$) will be kept constant, along with SJ pulsating frequency ($f_0 = 7.1\ Hz$) ($F^+ = 1$), the groove position ($x/C = 0.4$), and width ($h = 0.5\%C$). Ten different jet inclination angles ranging between 2 and 50 degrees were simulated. Table 7 presents the time-averaged values for the aerodynamic coefficients and their respective peak-to-peak amplitudes corresponding to each jet angular position evaluated. From these data, it is highlighted that the optimal angle obtained from the parametric optimization is $\theta_{\text{jet}} = 5$ deg., with its associated efficiency of $\eta = 41.067$; however, it should be mentioned that $\theta_{\text{jet}} = 2$ deg. yields a higher lift coefficient, although the efficiency drastically decays to $\eta = 16.151$. Concerning the oscillations of the lift and drag coefficients in relation to the jet angle, it can be observed that the lift coefficient's PTP values remain relatively stable for injection angles below 25 degrees. Furthermore, in the case of the drag coefficient, oscillations decrease notably within the region of minimum drag, specifically within the range of jet angles where $5 \leq \theta_{\text{jet}} \leq 20$. The observed reduction in PTP values for both lift and drag coefficients, see Table 7, signifies an improvement in the dynamic forces, which reduce vibration when compared with the baseline case.

When exploring the lift coefficient as a function of the jet angle in Figure 11a, it is observed that the lift keeps increasing as the jet angle decreases, suggesting a delay of the boundary layer separation. Additionally, studies such as [58–60] have extensively explored the effects of tangential flow injection and have demonstrated its ability to promote flow reattachment and lift increase. The Coanda effect refers to the tendency of a fluid jet to adhere to a nearby surface due to the curvature of the solid body. By decreasing the jet angle, the airflow is directed closer to the airfoil surface, effectively leveraging the Coanda effect to enhance boundary layer reattachment. Thus, regarding the results obtained in this research, the observed increase in lift coefficient with decreasing jet angle aligns with the predictable outcomes of previous research.



(**a**) (**b**) (**c**)

Figure 11. Lift coefficient (**a**), drag coefficient (**b**), and aerodynamic efficiency (**c**) variation as a function of the jet angle; the vertical bars characterize the corresponding peak-to-peak amplitude. Constant momentum coefficient ($C_\mu = 0.007$) and forcing frequency ($F^+ = 1$).

Table 7. Time-averaged aerodynamic coefficients C_l, C_d, and η, and their respective peak-to-peak values PTP_{C_l} and PTP_{C_d}, for a set of different jet inclination angles θ_{jet}. Momentum coefficient ($C_\mu = 0.007$), forcing frequency ($F^+ = 1$), groove position ($x/C = 0.4$), and width ($h = 0.5\%C$) are kept constant.

θ_{jet}	C_l	C_d	η	PTP_{C_l}	PTP_{C_d}
2	2.633	0.163	16.151	0.163	0.087
5	2.537	0.062	41.067	0.090	0.050
7	2.490	0.057	43.510	0.085	0.041
10	2.450	0.050	48.712	0.114	0.046
15	2.345	0.052	45.297	0.092	0.035
20	2.249	0.057	39.114	0.110	0.036
25	2.225	0.066	33.505	0.110	0.070
30	2.242	0.063	35.466	0.075	0.028
40	2.033	0.082	24.795	0.309	0.111
50	2.079	0.070	29.592	0.095	0.036
BCS S54	1.562	0.106	14.71	0.281	0.104

When considering the choice of $\theta_{\text{jet}} = 5$ deg. as the optimal jet angle for the AFC implementation, it is essential to examine the effects on drag coefficient and aerodynamic efficiency, Figures 11b and 11c, respectively. The drag coefficient remains relatively low for most of the studied jet angles; however, as the injection direction approaches tangential flow, the drag coefficient experiences a notable increase, even higher than the baseline case, leading to a rapid decrease in aerodynamic efficiency. Considering the airfoil efficiency in Figure 11c and Table 7, it is obvious that the maximum efficiency is obtained at $\theta_{jet} = 10°$, but as explained before, the final jet inclination angle chosen is based on a trade-off between maximum lift and maximum efficiency.

4.5. Forcing Frequency Optimization

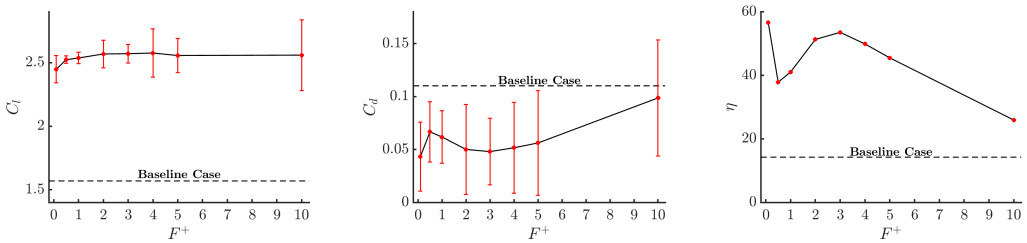
At this point, the two previously optimized AFC parameters, momentum coefficient $C_\mu = 0.007$ and jet angle $\theta_{\text{jet}} = 5$ deg., are going to be held constant. Being the remaining parameter to be optimized, the jet pulsating frequency f. Eight different non-dimensional frequencies are analyzed in this part of the study; their values range between $0.1 \leq F^+ \leq 10$. The results obtained after the corresponding CFD simulations are presented in Table 8, where the baseline case data are introduced in the last line for comparison. Based on the information presented, it can be concluded that the optimal value for the jet non-dimensional forcing frequency is $F^+ = 3$. This choice is supported by the highest lift-to-drag ratio, excellent lift capabilities C_l, and a particularly low drag coefficient C_d.

Figure 12a is presenting the lift coefficient and its peak-to-peak amplitude for the different pulsating frequencies evaluated. The first thing to observe is that variations of the pulsating frequency are slightly modifying the lift; a small decrease in lift is observed when considering the smallest forcing frequencies. However, once the forcing frequency reaches approximately $F^+ = 2$, the lift coefficient remains relatively constant suggesting that the optimal value for the forcing frequency should be greater than 2 ($F^+ \geq 2$). Moreover, it is important to mention that at higher forcing frequencies, the peak-to-peak values for the lift coefficient increase significantly, which indicates the presence of larger amplitude fluctuations and thus, higher structural loads. When checking the drag coefficient values obtained at the different pulsating frequencies evaluated, Figure 12b shows minimum drag values are observed at $F^+ = 0.1$ and around $F^+ = 3$. It therefore seems that an analysis of the aerodynamic efficiency needs to be made in order to determine the optimal forcing frequency. From Figure 12c it can be seen that there is a high aerodynamic efficiency at $F^+ = 0.1$, although it will not be chosen as the optimal value due to its lower lift coefficient. In contrast, regarding the remaining values for frequency, there is an efficiency peak at $F^+ = 3$, which offers a significant increase in lift coefficient, leading to an increase in torque generation while maintaining a low drag coefficient (see Figure 12b). Additionally, the amplitude of oscillation at this frequency is relatively low, suggesting that it will

have minimal impact on structural loads. It is relevant to highlight that the optimization methodology just introduced may not generate the optimum AFC values, but it allows obtaining rather close ones.

Table 8. Time-averaged aerodynamic coefficients C_l, C_d, and η, and their respective peak-to-peak PTP_{C_d} and PTP_{C_d} amplitude, as a function of the SJ non-dimensional pulsating frequency. Momentum coefficient ($C_\mu = 0.007$), jet angle ($\theta_{\text{jet}} = 5$ deg.), groove position ($x/C = 0.4$), and width ($h = 0.5\%C$), are kept constant.

F^+	C_l	C_d	η	PTP_{C_l}	PTP_{C_d}
0.1	2.499	0.043	56.643	0.214	0.065
0.5	2.524	0.067	37.856	0.059	0.057
1	2.537	0.062	41.067	0.090	0.050
2	2.569	0.050	51.325	0.218	0.085
3	2.571	0.048	53.563	0.147	0.063
4	2.576	0.052	49.897	0.381	0.086
5	2.557	0.056	45.532	0.269	0.099
10	2.560	0.099	25.932	0.557	0.110
BCS S54	1.562	0.106	14.71	0.281	0.104



(**a**) (**b**) (**c**)

Figure 12. Lift coefficient (**a**), drag coefficient (**b**), and aerodynamic efficiency (**c**) variation as a function of forcing frequency; the vertical bars characterize the corresponding peak-to-peak amplitude. Constant momentum coefficient ($C_\mu = 0.007$) and jet angle ($\theta_{\text{jet}} = 5$ deg.).

4.6. Velocity and Pressure Fields for the Optimal θ, C_μ, and F^+ Values

In the present section, the streamlines, contours, and the pressure fields for the baseline case and the optimum AFC parameters implementation obtained from the parametric optimization are compared in Figure 13. It is evident that the AFC implementation has effectively reattached the flow on the entire airfoil and so has been able to maximize its aerodynamic performance. The location of the SJA is defined in Figure 13b. A comparison of the pressure contour fields between the baseline and the optimum actuated case shows a much larger low-pressure area on the airfoil upper surface than the one observed for the baseline case, therefore explaining the effect of the actuation on the pressure field and the associated lift increase, which is of 64.59%. It is as well remarkable to highlight the lift peak-to-peak amplitude reduction when applying AFC, such reduction being of 47.6%. This considerable boost in lift performance seen in Table 8 will be later used for the energy assessment and torque improvement of the DTU 10MW RWT. Remarkable improvements can also observed in the drag coefficient when comparing the actuated case with the baseline case. Specifically, there has been a notable reduction in this parameter, amounting to an averaged decrease by 54.71%. Moreover, the drag peak-to-peak amplitude has decreased a 39.42% when compared with that of the baseline case. Such lift and drag peak-to-peak values decrease is extremely beneficial when considering the life expectancy of any WT, then sharply reduce the potential vibrations that could impact the blade. To determine the effects of these oscillatory drag and lift coefficients, a comprehensive structural analysis is required; however, it is out of the scope of the present work. The aerodynamic efficiency, as shown in Table 8, clearly demonstrates the positive impact of the AFC implementation on

the airfoil's lift-to-drag ratio. The reattachment of the flow, coupled with the increase in lift coefficient and the decrease in drag coefficient, has contributed to the mentioned significant efficiency improvement (264.12%).

The non-dimensional turbulence viscosity fields for the baseline case and the optimum AFC parameters implementation are introduced in Figure 14. The locations where the Reynolds stresses are particularly high, which are the airfoil trailing edge (for the AFC case) and the area where the boundary layer is separated as well as the downstream zone (for the baseline case), are now clearly observed. In fact, an inverse relationship between the lift generated by the airfoil section and the area covered by high-turbulence viscosity can be established. For the case of optimum AFC parameters implementation, it is now seen that small vortical structures are expected at the airfoil trailing edge; turbulence viscosity is particularly large at this point, highlighting the particularly large momentum interchange between the fluid particles. It appears as if the boundary layer was about to separate just before the airfoil trailing edge.

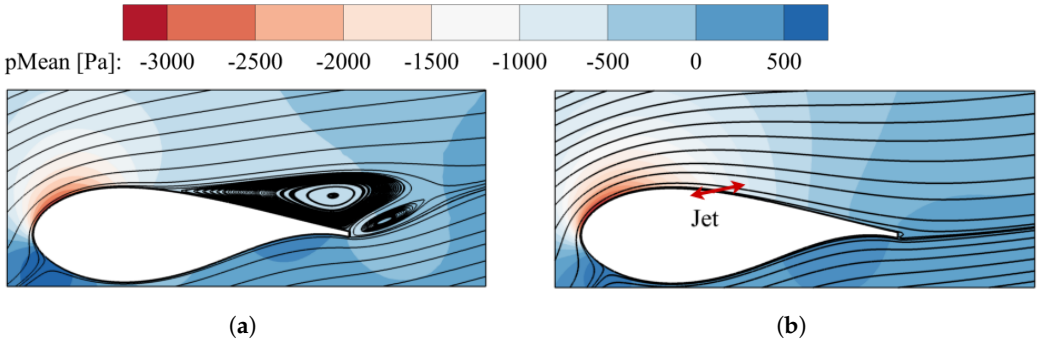


Figure 13. Streamlines of temporal average velocity field and contours of averaged pressure in Section 54 for the baseline case (**a**) and optimum AFC implementation case (**b**).

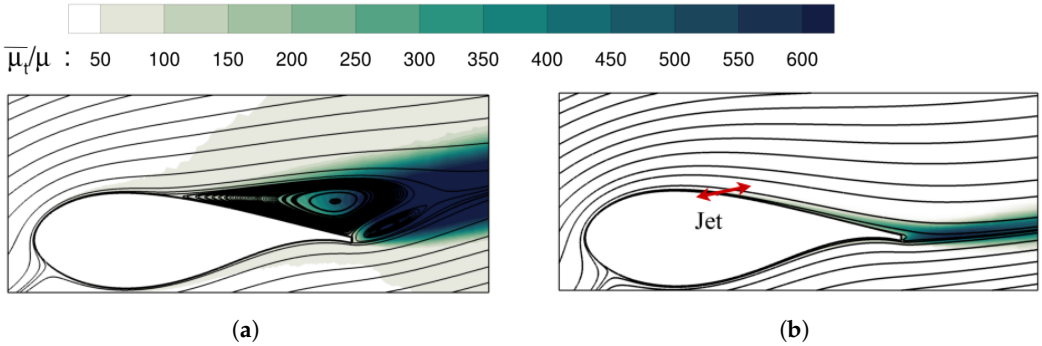


Figure 14. Streamlines of temporal average velocity field and contours of non-dimensional turbulence viscosity in Section 54 for the baseline case (**a**) and maximum lift case (**b**).

In order to further clarify the effect of the synthetic jet on the flow just downstream of the groove location, the SJ oscillation period has been divided into six equal time steps and presented in Figure 15. At the initial time shown in this figure, what we called time $(0/6)T$, the outgoing jet velocity is maximum, $u_{\text{jet}}(t) = u_{\text{max}}$, and the turbulence viscosity is particularly high at the jet exit and downstream of it. The streamlines are suffering a particularly high curvature under these conditions. As the outgoing jet velocity decreases, (1/6)T and (2/6)T, the streamlines curvature as well as the turbulent viscosity downstream of the injection area also decrease. When the suction phase starts (3/6)T, the streamlines just upstream of the jet location start bending inwards, with this bending curvature maximum at (4/6)T, which coincides with the maximum incoming jet velocity. The turbulence viscosity around the jet location during the suction phase appears to be particularly low.

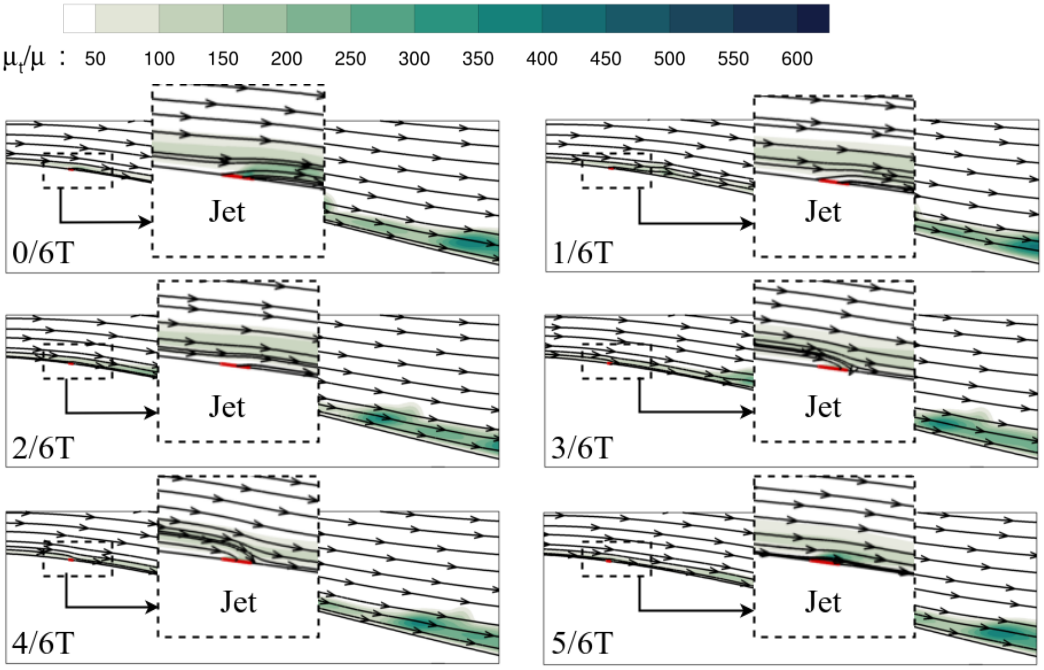
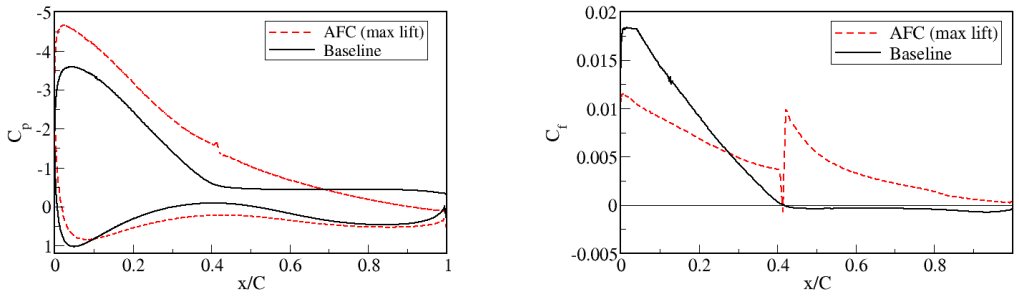


Figure 15. Instantaneous velocity streamlines and non-dimensional turbulence viscosity at different phases of the synthetic jet for the maximum lift case in Section 54. $F^+ = 3$, $C_\mu = 0.007, \theta = 5°$.

The pressure coefficient analysis, as shown in Figure 16a, provides insights into the behavior of the actuated and baseline cases, and a comparison between the two reveals notable differences. In the actuated case, there is an evident increase in the suction peak near the leading edge in reference to the baseline case. Moreover, the pressure recovery on the upper surface of the airfoil is smooth, indicating the absence of flow separation. This is in contrast to the baseline case, which exhibits a sharp gradient of the pressure coefficient, suggesting the presence of separated flow. Notice as well that the pressure below the airfoil is higher in the AFC case than in the baseline one. The analysis of the tangential friction coefficient (C_f) in Figure 16b provides valuable insights into the flow behavior along the airfoil's surface. In the case of the AFC implementation, it is observed that the SJ generates a sudden rise of the friction coefficient, which prevents it from becoming negative at any point along the chord of the airfoil, which suggests that the flow remains attached throughout the entire airfoil. In contrast, in the baseline case, flow separation is clearly observed at $x/c = 0.423$.

Figure 17 provides a comparison between the time-averaged velocity profiles tangent to the airfoil for both the AFC (actuated) and baseline cases. Regarding the AFC case, it is observed that the velocity distribution is positive at all points, therefore matching the profile of a non-separated flow. Moreover, the increase in velocity near the jet injection region is clearly visible, indicating the impact of the synthetic jet on the external flow. On the other hand, the baseline case exhibits a negative velocity distribution pattern from $x/c = 0.423$ to $x/c = 1$, indicating the occurrence of flow separation in all this zone.



(**a**) (**b**)

Figure 16. Pressure and tangential wall shear stress coefficients between the baseline case and the optimal AFC implementation on Section 54.

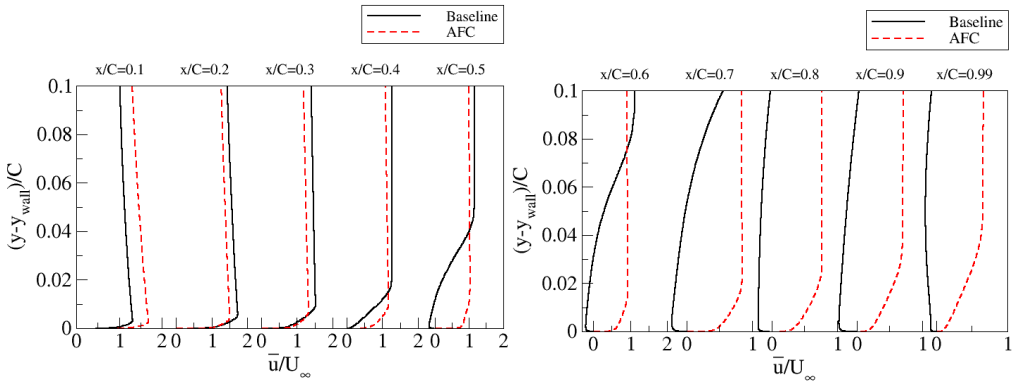


Figure 17. Mean velocity profiles tangent to the airfoil surface at several streamwise locations, from $x/C = 0.1$ to $x/C = 0.99$, and as a function of the normalized wall normal distance. Comparison of the baseline with the optimum AFC case.

4.7. Energy Assessment

The present section determines the energy gained by the AFC implementation in Section 54. The power required by the synthetic jet to delay the boundary layer separation is compared with the power increase obtained from this airfoil section due to the AFC implementation and considering an airfoil span of 1m. The power required to activate the synthetic jet is defined as follows [19,22]:

$$W_j = \frac{1}{2}\rho_j A_j \sin\theta_{\text{jet}} \overline{u_j^3} \tag{32}$$

where ρ_j states for the density of the exiting fluid (in this case air at sea level ISA conditions, $\rho_j = \rho_\infty = 1.225\,\text{kg/m}^3$), A_j is the cross-sectional flow area of the synthetic jets ($A_j = h \cdot \text{extrusion length} = h \cdot 1 = 0.03045\,m$) and $\overline{u_j^3}$ is the jet time dependent velocity profile defined as follows [19,61]:

$$\overline{u_j^3} = \frac{1}{T/2}\int_0^{T/2} u_{\max}^3 \sin^3(2\pi f t)\mathrm{d}t = \frac{4}{3\pi}u_{\max}^3 \tag{33}$$

T being the SJ oscillation period.

The incremental torque represents the difference between the torque generated by the actuated section and the baseline one. It is initially essential to determine the resultant aerodynamic force (F_{rot}) for both cases, which is obtained by decomposing the lift and drag

forces in the plane of rotation using the inflow angle (φ). It is important to note that the provided aerodynamic coefficients are time-averaged values, ensuring a representative analysis of the aerodynamic forces.

$$F_{rot\,AFC} = \frac{1}{2}\rho_\infty u_{rel}^2 c(c_{l\,AFC}\sin\varphi - c_{d\,AFC}\cos\varphi) \tag{34}$$

$$F_{rot\,BSC} = \frac{1}{2}\rho_\infty u_{rel}^2 c(c_{l\,BCS}\sin\varphi - c_{d\,BCS}\cos\varphi) \tag{35}$$

By considering the forces generated by the airfoil section in both the actuated and baseline cases, the increase in torque ΔQ can be determined.

$$\Delta Q = Q_{AFC} - Q_{BCS} = z_{S54}\cdot(F_{rot\,AFC} - F_{rot\,BCS}) \tag{36}$$

z_{S54} represents the z coordinate of the improved section, its value being 31.42 m.

At this stage, the increase in output power resulting from the lift and drag improvement on the studied airfoil section can be expressed as follows,with Ω denoting the wind turbine angular velocity in radians per second (rad/s).

$$\Delta W = \Delta Q\cdot\Omega \tag{37}$$

To evaluate the net power (W_G) obtained by the AFC implementation on the studied airfoil section and when considering a span of 1m, the power needed to delay the boundary layer separation on this section (W_j) must be considered; the resulting equation reads

$$W_G = \Delta W - W_j \tag{38}$$

The numerical values for the previous equation give the following:

$$W_G = 27.982 - 1.794 = 26.188\,\text{kW} \tag{39}$$

If W_G becomes negative, it means that the AFC implementation could improve the lift and aerodynamic efficiency of the section but without a net power saving to the theoretical wind turbine composed of this single airfoil section. In contrast, whenever the power balance becomes positive, there is a gain in total energy and enhanced aerodynamic capabilities of the mentioned section. In the current case, the power required by the synthetic jet to fully attach the flow to the airfoil represents 6.41 % of the power gained resulting from the increased lift and reduced drag achieved through the AFC implementation. Therefore, it can be concluded that the AFC implementation via synthetic jets on Section 54 (DTU 10MW RWT) at a wind speed of 10 m/s greatly increases the power output of a theoretical wind turbine composed of this single section having a span of 1m. The present study needs to be performed on the rest of the DTU 10MW RWT airfoil sections where the boundary layer is separated to be able to properly determine the power gain this particular WT could obtain at the studied wind speed.

5. Conclusions

This paper clarifies that to be able to improve the performance/efficiency/power generated in any wind turbine, it is essential to analyze the flow around each airfoil, including not just the aerodynamic forces (which is what has been conducted until now) but also the boundary layer separation point and the vortex shedding frequency/ies associated. Once this first step is accomplished, the flow can be reattached in any section via the use of AFC. The present research presents a parametric analysis with the aim to optimize three AFC parameters, the momentum coefficient, jet inclination angle, and pulsating frequency, associated with an SJA and when applied to a wind turbine section. The procedure followed to perform a parametric optimization of any airfoil is established and presented. A maximum airfoil efficiency increase versus the baseline case of 264% is obtained for C_μ = 0.007; F^+ = 3,

and $\theta_{jet} = 5°$ and when the groove was located at $x/C = 0.4269$, being its width of $0.005C$. The paper further proves that the AFC implementation, in a single airfoil section so far and thanks to the parametric optimization performed, requires about 6.4% of the energy increase experienced by the turbine due to the implementation of the AFC technique outlined in this paper. The peak-to-peak amplitude reduction of the time-dependent lift and drag coefficients versus the baseline case clearly indicates that the fluctuation forces on the blade can be drastically decreased when AFC is applied.

Author Contributions: Conceptualization, J.M.B.; methodology, M.L. and A.N.; software, M.L., M.S., and A.N.; validation, M.L., M.S., A.N., and J.M.B.; formal analysis, M.L., M.S., and A.N.; investigation, M.L., M.S., A.N., and J.M.B.; data curation, M.L., M.S., and A.N.; writing—original draft preparation, J.M.B., M.L., and A.N.; writing—review and editing, M.L., A.N., and J.M.B.; visualization, M.L., M.S., and A.N.; supervision, J.M.B.; project administration, J.M.B. All authors have read and agreed to the published version of the manuscript.

Funding: This research was supported by the Universitat Politècnica de Catalunya under the grant OBLEA-2024 and by the Spanish Ministerio de Ciencia, Innovacion y Universidades with the project PID2023-150014OB-C21. Some of the computations were performed in the Red Española de Supercomputación (RES), the Spanish supercomputer network, under the grant IM-2024-2-0008.

Institutional Review Board Statement: Not applicable.

Informed Consent Statement: Not applicable.

Data Availability Statement: Data are contained within the article.

Conflicts of Interest: The authors declare no conflicts of interest.

References

1. Zhu, H.; Hao, W.; Li, C.; Ding, Q. Simulation on flow control strategy of synthetic jet in an vertical axis wind turbine. *Aerosp. Sci. Technol.* **2018**, *77*, 439–448. [CrossRef]
2. Hochhäusler, D.; Erfort, G. Experimental study on an airfoil equipped with an active flow control element. *Wind Eng.* **2021**, *46*, 1080–1093. [CrossRef]
3. Khalil, K.; Asaro, S.; Bauknecht, A. Active flow control devices for wing load alleviation. *J. Aircr.* **2021**, *59*, 458–473. [CrossRef]
4. Mosca, V.; Karpuk, S.; Sudhi, A.; Badrya, C.; Elham, A. Multidisciplinary design optimisation of a fully electric regional aircraft wing with active flow control technology. *Aeronaut. J.* **2021**, *126*, 730–754. [CrossRef]
5. Maldonado, V.; Peralta, N.; Ayele, W.; Santos, D.; Dufflis, G. Effect of blade aspect ratio on the performance tradeoff between figure of merit and bending-torsion dynamics of wind turbines with synthetic jets. *Energy Rep.* **2023**, *9*, 4830–4843. [CrossRef]
6. Cattafesta, L.N.; Sheplak, M. Actuators for Active Flow Control. *Annu. Rev. Fluid Mech.* **2011**, *43*, 247–272. [CrossRef]
7. Wang, L.; bao Tian, F. Numerical simulation of flow over a parallel cantilevered flag in the vicinity of a rigid wall. *Phys. Rev. E* **2019**, *99*, 053111. [CrossRef]
8. Cho, Y.C.; Shyy, W. Adaptive flow control of low-Reynolds number aerodynamics using dielectric barrier discharge actuator. *Prog. Aerosp. Sci.* **2011**, *47*, 495–521. [CrossRef]
9. Foshat, S. Numerical investigation of the effects of plasma actuator on separated laminar flows past an incident plate under ground effect. *Aerosp. Sci. Technol.* **2020**, *98*, 105646. [CrossRef]
10. Benard, N.; Moreau, E. Electrical and mechanical characteristics of surface AC dielectric barrier discharge plasma actuators applied to airflow control. *Exp. Fluids* **2014**, *55*, 1846. [CrossRef]
11. Benard, N.; Pons-Prats, J.; Periaux, J.; Bugeda, G.; Braud, P.; Bonnet, J.; Moreau, E. Turbulent separated shear flow control by surface plasma actuator: Experimental optimization by genetic algorithm approach. *Exp. Fluids* **2016**, *57*, 22. [CrossRef]
12. Bergadà, J.M.; Baghaei, M.; Prakash, B.; Mellibovsky, F. Fluidic Oscillators, Feedback Channel Effect under Compressible Flow Conditions. *Sensors* **2021**, *21*, 5768. [CrossRef] [PubMed]
13. Baghaei, M.; Bergada, J.M. Fluidic Oscillators, the Effect of Some Design Modifications. *Appl. Sci.* **2020**, *10*, 2105. [CrossRef]
14. Baghaei, M.; Bergada, J.M. Analysis of the Forces Driving the Oscillations in 3D Fluidic Oscillators. *Energies* **2019**, *12*, 4720. [CrossRef]
15. Glezer, A.; Amitay, M. Synthetic jets. *Annu. Rev. Fluid Mech.* **2002**, *34*, 503–529. [CrossRef]
16. Rumsey, C.; Gatski, T.; Sellers, W.; Vatsa, V.; Viken, S. Summary of the 2004 CFD validation workshop on synthetic jets and turbulent separation control. In Proceedings of the 2nd AIAA Flow Control Conference, Portland, OR, USA, 28 June–1 July 2004; p. 2217.
17. Wygnanski, I. The variables affecting the control of separation by periodic excitation. In Proceedings of the 2nd AIAA Flow Control Conference, Portland, OR, USA, 28 June–1 July 2004; p. 2505.

18. Findanis, N.; Ahmed, N. The interaction of an asymmetrical localised synthetic jet on a side-supported sphere. *J. Fluids Struct.* **2008**, *24*, 1006–1020. [CrossRef]
19. De Giorgi, M.; De Luca, C.; Ficarella, A.; Marra, F. Comparison between synthetic jets and continuous jets for active flow control: Application on a NACA 0015 and a compressor stator cascade. *Aerosp. Sci. Technol.* **2015**, *43*, 256–280. [CrossRef]
20. Traficante, S.; De Giorgi, M.; Ficarella, A. Flow separation control on a compressor-stator cascade using plasma actuators and synthetic and continuous jets. *J. Aerosp. Eng.* **2016**, *29*, 04015056. [CrossRef]
21. Zhang, H.; Chen, S.; Gong, Y.; Wang, S. A comparison of different unsteady flow control techniques in a highly loaded compressor cascade. *Proc. Inst. Mech. Eng. Part G J. Aerosp. Eng.* **2019**, *233*, 2051–2065. [CrossRef]
22. Tousi, N.M.; Coma, M.; Bergada, J.M.; Pons-Prats, J.; Mellibovsky, F.; Bugeda, G. Active Flow Control Optimisation on SD7003 Airfoil at Pre and Post-stall Angles of Attack using Synthetic Jets. *Appl. Math. Model.* **2021**, *98*, 435–464. : 10.1016/j.apm.2021.05.016 [CrossRef]
23. Tadjfar, M.; Kamari, D. Optimization of Flow Control Parameters Over SD7003 Airfoil With Synthetic Jet Actuator. *J. Fluids Eng.* **2020**, *142*, 021206. [CrossRef]
24. Tousi, N.; Bergadà, J.; Mellibovsky, F. Large Eddy Simulation of optimal Synthetic Jet Actuation on a SD7003 airfoil in post-stall conditions. *Aerosp. Sci. Technol.* **2022**, *127*, 107679. [CrossRef]
25. Stalnov, O.; Kribus, A.; Seifert, A. Evaluation of active flow control applied to wind turbine blade section. *J. Renew. Sustain. Energy* **2010**, *2*, 063101. [CrossRef]
26. Maldonado, V.; Farnsworth, J.; Gressick, W.; Amitay, M. Active control of flow separation and structural vibrations of wind turbine blades. *Wind Energy Int. J. Prog. Appl. Wind Power Convers. Technol.* **2010**, *13*, 221–237. [CrossRef]
27. Yen, J.; Ahmed, N.A. Enhancing vertical axis wind turbine by dynamic stall control using synthetic jets. *J. Wind Eng. Ind. Aerodyn.* **2013**, *114*, 12–17. [CrossRef]
28. Taylor, K.; Leong, C.M.; Amitay, M. Load control on a dynamically pitching finite span wind turbine blade using synthetic jets. *Wind Energy* **2015**, *18*, 1759–1775. [CrossRef]
29. Velasco, D.; Mejia, O.L.; Laín, S. Numerical simulations of active flow control with synthetic jets in a Darrieus turbine. *Renew. Energy* **2017**, *113*, 129–140. [CrossRef]
30. Moshfeghi, M.; Hur, N. Numerical study on the effects of a synthetic jet actuator on S809 airfoil aerodynamics at different flow regimes and jet flow angles. *J. Mech. Sci. Technol.* **2017**, *31*, 1233–1240. [CrossRef]
31. Maldonado, V.; Gupta, S. Increasing the power efficiency of rotors at transitional Reynolds numbers with synthetic jet actuators. *Exp. Therm. Fluid Sci.* **2019**, *105*, 356–366. [CrossRef]
32. Wang, P.; Liu, Q.; Li, C.; Miao, W.; Luo, S.; Sun, K.; Niu, K. Effect of trailing edge dual synthesis jets actuator on aerodynamic characteristics of a straight-bladed vertical axis wind turbine. *Energy* **2022**, *238*, 121792. [CrossRef]
33. Maldonado, V.; Boucher, M.; Ostman, R.; Amitay, M. Active Vibration Control of a Wind Turbine Blade Using Synthetic Jets. *Int. J. Flow Control* **2009**, *1*, 227–238. [CrossRef]
34. Goodfellow, S.D.; Yarusevych, S.; Sullivan, P.E. Momentum Coefficient as a Parameter for Aerodynamic Flow Control with Synthetic Jets. *AIAA J.* **2013**, *51*, 623–631. [CrossRef]
35. Feero, M.A.; Lavoie, P.; Sullivan, P.E. Influence of synthetic jet location on active control of an airfoil at low Reynolds number. *Exp. Fluids* **2017**, *58*, 99. [CrossRef]
36. Amitay, M.; Smith, D.R.; Kibens, V.; Parekh, D.E.; Glezer, A. Aerodynamic flow control over an unconventional airfoil using synthetic jet actuators. *AIAA J.* **2001**, *39*, 361–370. [CrossRef]
37. Amitay, M.; Glezer, A. Role of actuation frequency in controlled flow reattachment over a stalled airfoil. *AIAA J.* **2002**, *40*, 209–216. [CrossRef]
38. Feero, M.A.; Goodfellow, S.D.; Lavoie, P.; Sullivan, P.E. Flow Reattachment Using Synthetic Jet Actuation on a Low-Reynolds-Number Airfoil. *AIAA J.* **2015**, *53*, 2005–2014. [CrossRef]
39. Tuck, A.; Soria, J. Separation control on a NACA 0015 airfoil using a 2D micro ZNMF jet. *Aircr. Eng. Aerosp. Technol.* **2008**, *80*, 175–180. [CrossRef]
40. Kitsios, V.; Cordier, L.; Bonnet, J.P.; Ooi, A.; Soria, J. On the coherent structures and stability properties of a leading-edge separated aerofoil with turbulent recirculation. *J. Fluid Mech.* **2011**, *683*, 395–416. [CrossRef]
41. Buchmann, N.; Atkinson, C.; Soria, J. Influence of ZNMF jet flow control on the spatio-temporal flow structure over a NACA-0015 airfoil. *Exp. Fluids* **2013**, *54*, 1485. [CrossRef]
42. Zhang, W.; Samtaney, R. A direct numerical simulation investigation of the synthetic jet frequency effects on separation control of low-Re flow past an airfoil. *Phys. Fluids* **2015**, *27*, 055101. [CrossRef]
43. Kim, S.H.; Kim, C. Separation control on NACA23012 using synthetic jet. *Aerosp. Sci. Technol.* **2009**, *13*, 172–182. [CrossRef]
44. Monir, H.E.; Tadjfar, M.; Bakhtian, A. Tangential synthetic jets for separation control. *J. Fluids Struct.* **2014**, *45*, 50–65. [CrossRef]
45. Cai, W.; Hu, Y.; Fang, F.; Yao, L.; Liu, J. Wind farm power production and fatigue load optimization based on dynamic partitioning and wake redirection of wind turbines. *Appl. Energy* **2023**, *339*, 121000. [CrossRef]
46. Silva, J.G.; Ferrari, R.; van Wingerden, J.W. Wind farm control for wake-loss compensation, thrust balancing and load-limiting of turbines. *Renew. Energy* **2023**, *203*, 421–433. [CrossRef]
47. Zagubień, A.; Wolniewicz, K.; Szwochertowski, J. Analysis of Wind Farm Productivity Taking Wake Loss into Account: Case Study. *Energies* **2024**, *17*, 5816. [CrossRef]

48. Menter, F. Zonal two equation kw turbulence models for aerodynamic flows. In Proceedings of the 23rd Fluid Dynamics, Plasmadynamics, and Lasers Conference, Orlando, FL, USA, 6–9 July 1993; p. 2906.
49. Menter, F.R. Two-equation eddy-viscosity turbulence models for engineering applications. *AIAA J.* **1994**, *32*, 1598–1605. [CrossRef]
50. Couto, N.; Bergada, J.M. Aerodynamic efficiency improvement on a NACA-8412 airfoil via active flow control implementation. *Appl. Sci.* **2022**, *12*, 4269. [CrossRef]
51. Bak, C.; Zahle, F.; Bitsche, R.; Kim, T.; Yde, A.; Henriksen, L.C.; Natarajan, A.; Hansen, M. *Description of the DTU 10 MW Reference Wind Turbine, DTU Wind Energy Report-I-0092*; Technical University of Denmark: Fredericia, Denmark, 2013.
52. Akon, A.F.; Samner, D.; Trovi, D. Measurement of Axial Induction Factor for a Model Wind Turbine. Ph.D. Thesis, Citeseer, Princeton, NJ, USA, 2012.
53. Zahle, F.; Bak, C.; Sørensen, N.N.; Guntur, S.; Troldborg, N. Comprehensive aerodynamic analysis of a 10 MW wind turbine rotor using 3D CFD. In Proceedings of the 32nd ASME Wind Energy Symposium, National Harbor, MD, USA, 13–17 January 2014; p. 0359.
54. Moriarty, P.J.; Hansen, A.C. *AeroDyn Theory Manual. Technical Report*; National Renewable Energy Lab.: Golden, CO, USA, 2005.
55. Mahmuddin, F. Rotor blade performance analysis with blade element momentum theory. *Energy Procedia* **2017**, *105*, 1123–1129. [CrossRef]
56. Bak, C.; Zahle, F.; Bitsche, R.; Kim, T.; Yde, A.; Henriksen, L.C.; Hansen, M.H.; Blasques, J.P.A.A.; Gaunaa, M.; Natarajan, A. The DTU 10-MW reference wind turbine. In Proceedings of the Danish Wind Power Research 2013, Fredericia, Denmark, 27–28 May 2013.
57. Meyers, R.A. *Encyclopedia of Physical Science and Technology*, 3rd ed.; Elsevier Science: Berkeley, CA, USA, 2001.
58. Tadjfar, M.; Asgari, E. The role of frequency and phase difference between the flow and the actuation signal of a tangential synthetic jet on dynamic stall flow control. *J. Fluids Eng.* **2018**, *140*, 111203. [CrossRef]
59. Krohnert, A. Numerical Investigation of Unsteady Tangential Blowing at the Rudder of a Vertical Tailplane Airfoil. In *New Results in Numerical and Experimental Fluid Mechanics X*; Contributions to the 19th STAB/DGLR Symposium, Munich, Germany; Springer: Berlin/Heidelberg, Germany, 2016; pp. 39–49.
60. Naim, A.; Greenblatt, D.; Seifert, A.; Wygnanski, I. Active control of a circular cylinder flow at transitional Reynolds numbers. *Flow Turbul. Combust.* **2007**, *78*, 383–407. [CrossRef]
61. De Giorgi, M.G.; Traficante, S.; De Luca, C.; Bello, D.; Ficarella, A. Active flow control techniques on a stator compressor cascade: A comparison between synthetic jet and plasma actuators. *Am. Soc. Mech. Eng.* **2012**, *44748*, 439–450.

Disclaimer/Publisher's Note: The statements, opinions and data contained in all publications are solely those of the individual author(s) and contributor(s) and not of MDPI and/or the editor(s). MDPI and/or the editor(s) disclaim responsibility for any injury to people or property resulting from any ideas, methods, instructions or products referred to in the content.